GSA Data Repository 2017276

Jourdan, F., et al., Collisional history of asteroid Itokawa: Geology, doi:10.1130/G39138.1.

SUPPLEMENTARY MATERIALS

Tables DR3-DR6

1. Petrography of the two particles.

Two dust particles were provided by JAXA (Japanese Aerospace Exploration Agency). Particles RA-QD02-0030 and RA-QD02-0013, hereafter named #0030 and #0013, respectively. Petrographic descriptions of the particles were provided by JAXA.

1.1 RA-QD02-0030

The size of the particle is 163.8 µm in its longer side (Fig. DR1). The main phase constituents are low-calcium pyroxene (56.1%), olivine (22 %), plagioclase (20%), taenite (0.25%) high-calcium pyroxene (1.5%) and troilite (0.13%) (Fig. DR2, DR3).

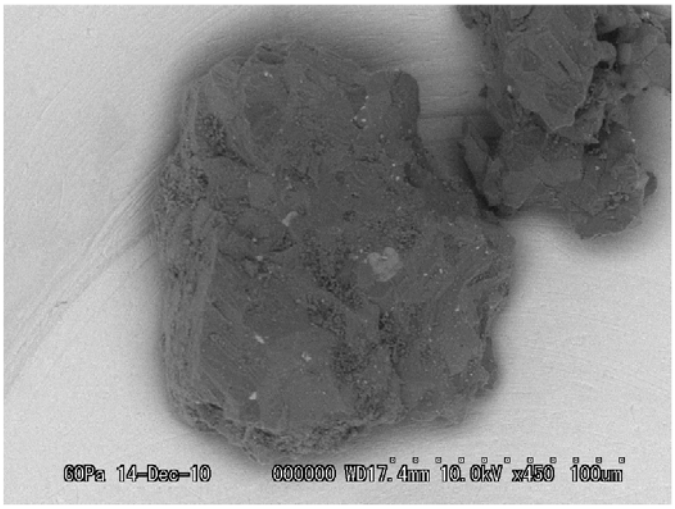

Fig. DR1*: SEM (Secondary Electron Microscope) picture of particle #0030 (courtesy of JAXA; (2011).*

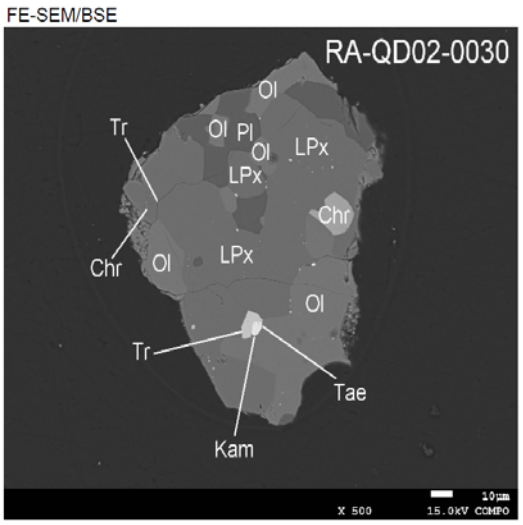

Fig. DR2: *Crystal phases of particle #0030 measured by SEM and EDX (Energy dispersion X-ray) imaging (courtesy of JAXA).*

The total volume of the particle is 760,531 um^3 and the porosity is 0.03%. The particle is equilibrated with an equilibration temperature calculated to be 636°C (Nakamura et al., 2011), consistent with petrologic type 5. The particle has been analysed for oxygen isotopes (Nakashima et al., 2013) and yielded ΔO^{17} values of 1.5 ± 0.4 ‰, typical for LL-chondrites.

The K_2O composition of the various phases is important for this study as $^{40}Ar/^{39}Ar$ dating depends on the quantity of K_2O from a sample, and to some extent the K_2O concentration in each of the phases. Table DR1 and Fig. DR3 give the K_2O concentration for each phase.

#0030

	Vol	K_2O	CaO	K	Ca	Ca/K	relative K	relative Ca	Particle Ca/K	%K tot
Plg	0.198	0.98	2.2	0.41	1.57	3.9	0.08	0.31		96.1%
Ol	0.224	0.01	0.01	0.00	0.01	1.7	0.00	0.00		1.1%
Kfeld	0									0.0%
LPX	0.561	0.01	0.9	0.00	0.64		0.002	0.36		2.8%
HPX	0.0142	0	0	0						0.0%
						total	0.08	0.67	**8.0**	

Table DR1: *K_2O concentration for each phase of particle #0030. Volume values are relative to each other for the particle. Units of K_2O, CaO, K and Ca are in weight %.*

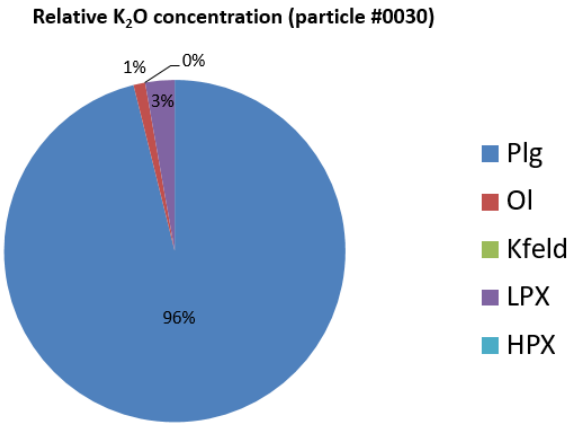

Fig. DR3: *relative K_2O concentration for each phase of particle #0030*

The relative K_2O concentrations plotted in Fig. DR3 show that the main contributor of radiogenic $^{40}Ar^*$ is plagioclase with 96% of the total K_2O, with low-Ca pyroxene and olivine accounting for the remaining 4% of the total.

1.2 RA-QD02-0013

The size of the particle is 91 µm in diameter and has an atypical rounded shape (Fig. DR4). The main phase constituents are olivine (53.5 vol%), plagioclase (33.96%), low-calcium pyroxene (5.76%), high-calcium pyroxene (4.4%) and Taenite (0.35%) and an exolution band of K-feldspar within plagioclase (Fig. DR5).

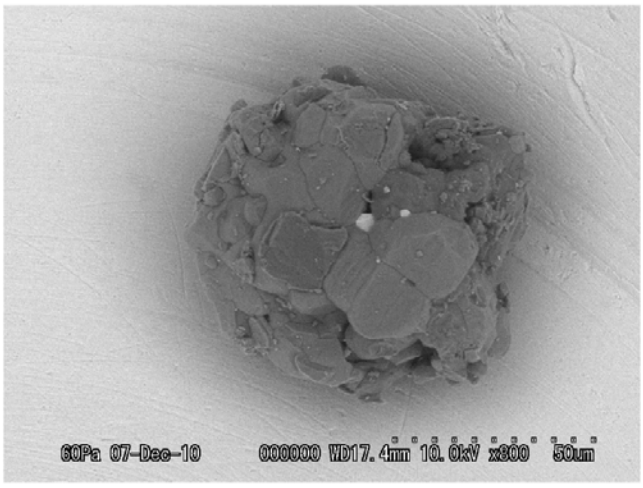

Fig. DR4: *SEM picture of particle #0030 (courtesy of JAXA)*

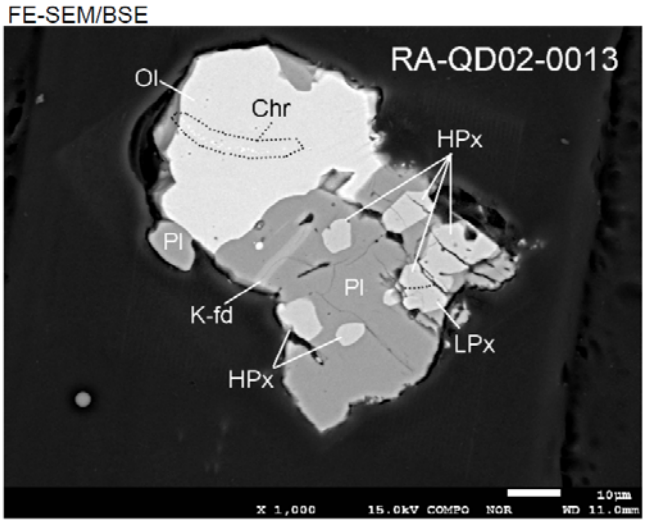

Fig. DR5: *Crystal phases of particle #0013 measured by SEM and EDX (courtesy of JAXA).*

The total volume of the particle is 234,404 um^3 and the porosity is 4.75%. Plagioclase triclinicity and QUILF pyroxene equilibrium calculations based on electronprobe data from of this particle suggest crystallization temperature of ca. 810-820°C (Nakamura et al., 2011) consistent with a petrologic type ≥5.

#0013

	Vol	K_20	CaO	K	Ca	Ca/K	relative K	relative Ca	Crystal Ca/K	%K tot
Plg	0.34	0.84	2.1	0.35	1.50	4.3	0.12	0.51		50.2%
Ol	0.535	0.01	0.01	0.00	0.01	1.7	0.00	0.00		0.9%
Kfeld	0.020	13.8	1.5	5.73	1.07	0.2	0.11	0.02		48.5%
LPX	0.057	0.02	0.9	0.01	0.64	77.5	0.000	0.04		0.2%
HPX	0.044	0.02	22.5	0.01	16.07	1936.81	0.00	0.71		0.2%
						total	0.24	1.28	**5.4**	

Table DR2: *K_2O concentration for each phase of particle #0013. Volume values are relative to each other for the particle. Units of K2O, CaO, K and Ca are in weight %.*

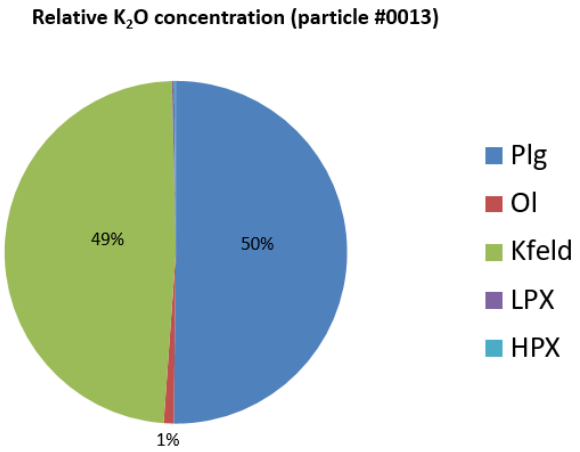

Fig. DR6: *relative K_2O concentration for each phase of particle #0013*

The relative K_2O concentrations (Table DR2) plotted in Fig. DR6 show that the main contributors of radiogenic $^{40}Ar^*$ are plagioclase and the small exolution lamellae of K-feldspar, with 50.2% and 48.5% of the total K_2O, respectively. Olivine and low and High with low-Ca pyroxene accounting for the remaining 1.3% of the total.

2. Analytical techniques

2.1 Electron Back Scatter Diffraction (EBSD)

Prior to EBSD analysis, the samples were polished for four hours with 0.6 μm colloidal silica in sodium hydroxide using a Buehler Vibromet II polisher in order to remove mechanical damage from previous polishing. The sample surface was monitored via optical microscopy every ten minutes during this polishing stage to ensure a high quality polish was achieved with minimal material loss. Pits from previous ion probe analyses (Nakashima et al., 2013; Yurimoto et al., 2011) remained visible after polishing, indicating that <1 μm of material was removed. A thin carbon coat was applied to mitigate charging in the scanning electron microscope (SEM).

EBSD data were collected on a Zeiss NEON 40 field emission (FE) SEM fitted with Oxford Instruments Channel 5 EBSD acquisition system and Nordlys 2 EBSD camera at Curtin University. SEM operating conditions were routine for EBSD analysis (20 kV acceleration voltage, 70° sample tilt, 15.0 mm working distance) (Prior et al., 1999). EBSD maps were collected using the Channel 5 Flamenco EBSD acquisition software using 60 ms pattern acquisition time, 64 frame background subtraction, 4x4 binning, Hough resolution of 65. Match units for forsterite, chromite, troilite, enstatite, and monoclinic (2/m) albite were used to index the EBSD patterns, which utilised 7 bands and band edges. The software was unable to distinguish taenite and kamacite, and so these phases were indexed using an FCC iron match unit. Indexing was not possible in remnant ion probe pits. Post-processing was done using Channel 5 Tango, and included removal of isolated erroneous points (wildspike correction) and systematically misindexed points, followed by zero solution extrapolation to 6 nearest neighbours. Comparison of the final data with band contrast map by visual inspection shows that no significant artefacts were generated.

Maps and pole figures were produced using Tango and Mambo modules in Channel 5 using available functions and routines in service pack 5.10. Pole figures are shown in the sample x-y-z reference frame, where x-y represents the plane of the polished surface. Pattern quality maps show that the surfaces of both particles are free of scratches and damage from previous polishing stages (Figs DR7, DR8).

2.1.1 Particle #0030

The proportion of successfully indexed points varied between phases, and generally related to EBSD pattern quality, particularly band contrast (Fig. DR7). Pattern quality and indexing of

the feldspar grains was particularly variable, and indexing was not possible for some of the plagioclase grains.

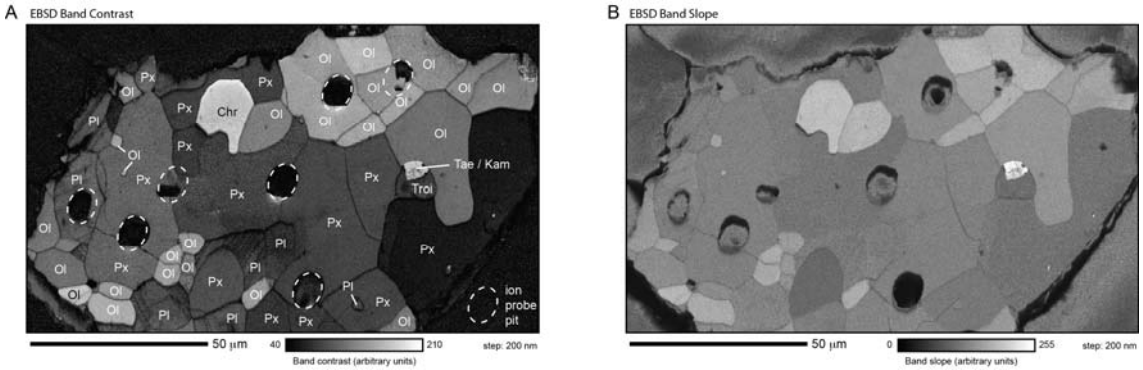

Fig. DR7*: Maps of particle #0030 shaded for different measures of EBSD pattern quality: (a) Band contrast. (b) Band slope.*

2.1.2 Particle #0013

The proportion of successfully indexed points varied between phases, and generally related to EBSD pattern quality, particularly band contrast (Fig. DR8). Pattern quality and indexing of the feldspar grains was significantly lower than in particle #0030, and indexing was not possible for the K-feldspar and some of the plagioclase grains.

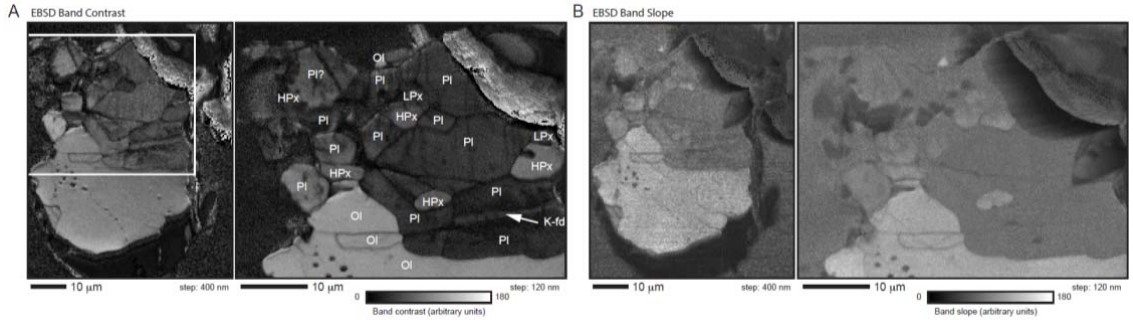

Fig. DR8*: Maps of particle #0013 shaded for different measures of EBSD pattern quality: (a) Band contrast. (b) Band slope.*

2.2 $^{40}Ar/^{39}Ar$ geochronology

2.2.1 Grain delivery and presentation on arrival

The two grains were shipped by JAXA and arrived individually mounted in resin stubs, polished to expose the grain and coated in carbon for the purpose of previous ion probe analysis. After removal of carbon coating (a possible contaminant for $^{40}Ar/^{39}Ar$ analyses) by

gently polishing the surface with ultra-fine diamond paste for hours, the grains were ready for extraction from the mount material.

Fig. DR9*: Microscope photographs of particles #0030 and #0013 within a mount and prior to extraction. The particles are embedded in resin and are carbon coated, as delivered by JAXA.*

2.2.2 Grain Removal experimentation and practice

The mount resin composition was provided by JAXA, and multi-part composite liquids were sourced to make samples of the same composition for us to mount test grains in and practice grain removal. Test mounts of varying hardness were prepared, containing grains of similar size and composition to the target grains. It was established that the mount resin was slightly elastic, and after softening the contact bond between the grains and the resin with a drop of acetone we found that a radial, outward-drawn star of scored lines around the mounted grains would stretch and open the "socket" of resin in which they were sunk, enabling the removal of the whole grain without any adhering mount material. Using this technique, the two Itokawa grains were removed from their stubs, and transferred on the tip of a probe to the individually prepared copper pits (Fig. DR10 and DR11). Grain movement and possible loss

was constrained by keeping the grain under a drop of liquid at all times; both on the stub and in the copper pit.

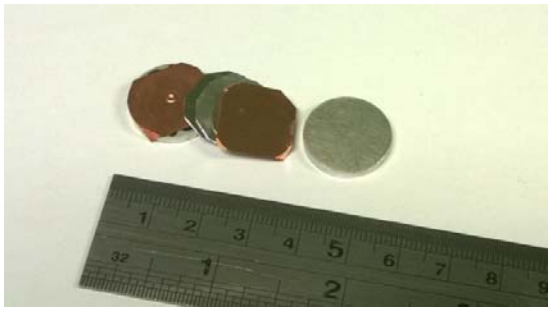

Fig. DR10*: Custom-made irradiation disc and plate setup used to carry a dust particle during the irradiation process.*

2.2.3 Grain packaging for irradiation

Tiny individual pits with a raised edge were prepared by embossing a small square of pure copper sheeting from behind (Fig. DR11). These were laid over the centre pit of a standard aluminium sample irradiation disc. Three separate hand-cut "washers" of cleaned aluminium foil were placed over the pit after the grain was placed inside, and a cover of flat copper closed the set. The disc was tightly lidded with a flat disc, which created downward pressure on the raised edge of the copper pit, further sealed by the malleable aluminium foil layers. The whole group was wrapped tightly in aluminium foil, and submitted to the reactor in the usual manner for irradiation (e.g., Jourdan et al., 2014).

Fig. DR11*: Particle #0030 after irradiation and before loading in the ARGUS VI extraction line.*

2.2.4 Irradiation and analytical procedures

Each disc included a series of Hb3gr hornblende used as a neutron fluence monitor for which an age of 1081.0 ± 1.0 Ma (1σ) was adopted (Renne et al., 2011) and a good in-between-grains reproducibility has been demonstrated (Jourdan and Renne, 2007; Jourdan et al., 2006). The discs were Cd-shielded (to minimize undesirable nuclear interference reactions) and irradiated for 50 hours in the US Geological Survey nuclear reactor (Denver, USA) in central position. The mean J-values computed from standard grains within small pits bracketing the particles yielded values of 0.008789 ± 0.000011 (0.125%) and 0.008651 ± 0.000024 (0.28%) for particle #0013 and #0030, respectively. Mass discrimination was monitored regularly through the analysis using an automated air pipette and provided a mean value of 0.99455 (± 0.05%) per dalton (atomic mass unit) relative to an air ratio of 298.56 ± 0.31 (Lee et al., 2006). The correction factors for interfering isotopes were $(^{39}Ar/^{37}Ar)_{Ca}$ = $7.06x10^{-4}$ (± 7%), $(^{36}Ar/^{37}Ar)_{Ca} = 2.81x10^{-4}$ (± 3%) and $(^{40}Ar/^{39}Ar)_{K} = 6.76x10^{-4}$ (± 10%).

The $^{40}Ar/^{39}Ar$ analyses were performed at the Western Australian Argon Isotope Facility at Curtin University. Test plagioclase crystals, standards and the two Itokawa particles were loaded in to a single laser disc. Test plagioclase crystals and the two particles were step-heated using a continuous 100 W PhotonMachine© CO_2 (IR, 10.4 µm) laser fired on the crystals during 30 seconds and the gas was purified on a single AP10 for a total of 180 seconds. Each standard crystal was fused in a single step a few months before the analyses of Itokawa's particles.

The gas was purified in an extra low-volume stainless steel extraction line of 170cc and using one SAES AP10 getter. Ar isotopes were measured in static mode using a low volume (600 cc) ARGUS VI mass spectrometer from Thermofisher© (Phillips and Matchan, 2013) set with a permanent resolution of ~200 (Fig. DR12). Measurements were carried out in peak jumping mode using a 0-background compact discrete dynode ion counter supplied with the ARGUS VI and using 10 cycles of peak-hopping and 33 seconds of integration time for each mass.

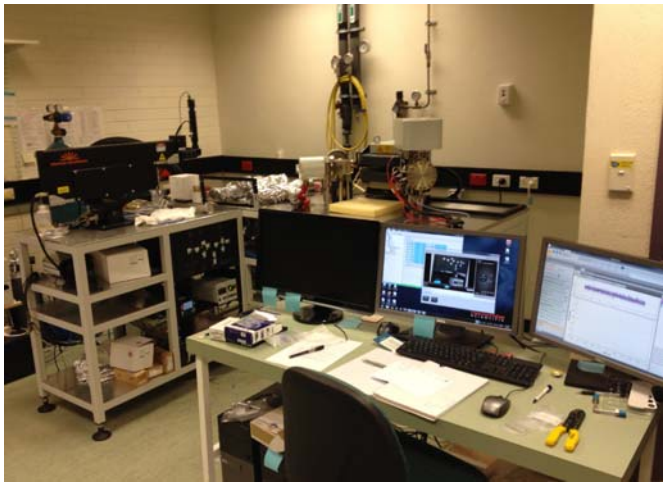

Fig. DR12: *ARGUS VI mass spectrometer and customized ultra-low volume extraction line at Curtin University.*

The raw data were processed using the ArArCALC software (Koppers, 2002) and the ages have been calculated using the decay constants recommended by Renne et al. (2011). Blanks were monitored every 3 to 4 steps and typical ^{40}Ar, ^{39}Ar and ^{36}Ar blank values of ca. 15.6, 0.016 and 0.056 fA. Relative abundance of Ar isotopic data of the two particles are provided in Annex 2 and have been corrected for blank, mass discrimination and radioactive decay are given in Annex 2. Individual errors in Annex 2 are given at the 1σ level.

Due to delay in the installation of the machine, the analyses of the two particles have been carried out more than a year after irradiation preventing measurement of ^{37}Ar for Ca interference correction. However, we used the Ca and K abundances measured by SEM and for each crystal types (Table DR1 and DR2) to calculate the Ca/K ratio of the particles and back calculate the ^{37}Ar content of each crystal based on mass ^{39}Ar. The calculated Ca/K values for particle #0030 and #0013 are 8.0 and 5.4 are in any case very low resulting in minimal interference corrections (Fig. DR13). No cosmogenic correction was attempted as the $^{38}Ar_{total}$ values remained at the blank level. Trapped intercept $^{40}Ar/^{36}Ar$ values was measured using the inverse isochron for sample #0013 and were applied to its age spectrum calculation, whereas it was assumed for particle #0030 due to the clustering of the data in the inverse isochron plot (Annexe 2).

Our criteria for the determination of plateau are as follows: plateaus must include at least 70% of ^{39}Ar. The plateau should be distributed over a minimum of 3 consecutive steps agreeing at 95% confidence level and satisfying a probability of fit (P) of at least 0.05. Plateau ages are given at the 2σ level and are calculated using the mean of all the plateau steps, each weighted by the inverse variance of their individual analytical error. Inverse isochrons include the maximum number of steps with a probability of fit ≥ 0.05. All sources of uncertainties are included in the calculation.

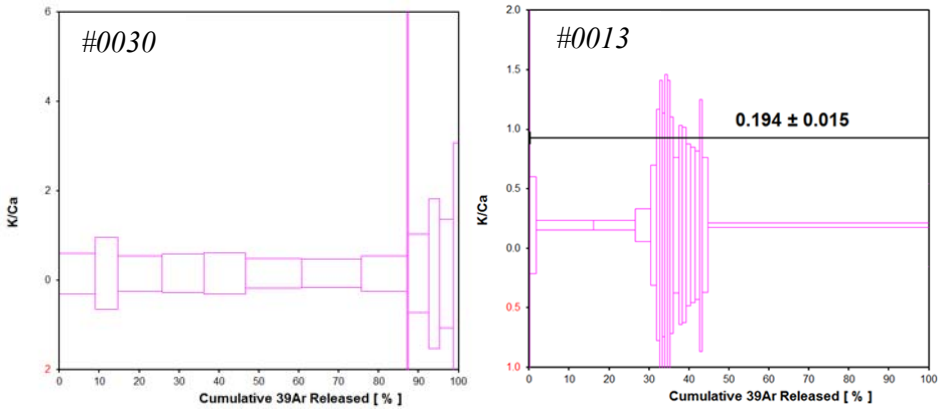

Fig. DR13: *K/Ca ratio plot of the particle #0030 and #0013 calculated based on the ^{39}Ar content and measured K and Ca content of the particle.*

3. Results

3.1.1 Particle RA-QD02-0030

EBSD analysis shows that larger, single phase domains in particle #0030 are polycrystals that comprise of smaller, interlocking, variably shaped grains (Fig. DR14). The grains are bound by high-angle (>10°) grain boundaries, with common curved boundary segments and 120° triple junctions (Fig. DR14). Grains from most phases (with the exception of plagioclase) contain no significant intragrain misorientations, i.e., are crystallographically continuous (Figs DR14 and DR15). Plagioclase grains preserve some twinning (Fig. DR14). Dispersion of data in pole figures show that two plagioclase grains preserve progressive orientation variations of up to 15°, misoriented around pole to {001} (Fig. DR15).

Pyroxene grains have a preferred crystallographic orientation (CPO), which is most pronounced by clustering of the {100}, {010} and {001} poles (Fig. DR15). No systematic CPOs are discernable for olivine or plagioclase, and there are too few grains of other phases to assess whether or not CPOs are present (Fig. DR15).

Fig. DR14: *EBSD maps coloured for (a) phase and (b) crystallographic orientation.*

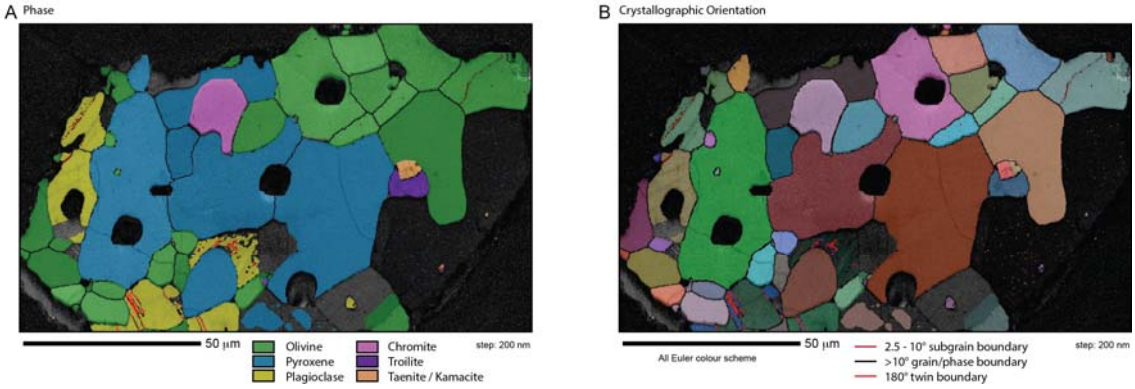

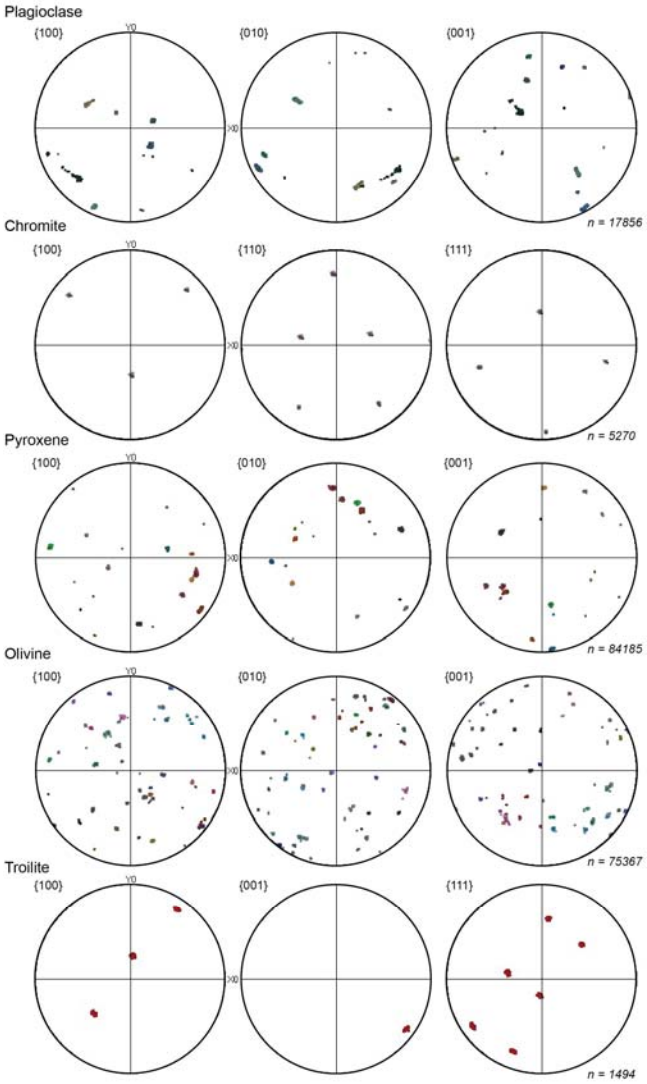

Fig. DR15*: Pole figures showing crystallographic orientation of data from different phases within particle #0030. Colours link to those shown in Fig. DR14B. Lower hemisphere, equal area stereographic projections.*

3.1.2 Particle RA-QD02-0013

Olivine, low-Ca pyroxene and high-Ca pyroxene indexed successfully, whereas the feldspars indexed with mixed success due to low EBSD pattern quality (Fig. DR16A). Indexing was not possible for the K-feldspar and some of the plagioclase grains due to low band contrast and band slope. Some plagioclase grains suffered from systematic misindexing that was difficult to eliminate during post-processing because these points have the same symmetry as twins (Fig. DR16B, red boundaries). Nevertheless, the EBSD maps show that the larger plagioclase domain comprises several smaller interlocking grains of plagioclase with no significant intragrain misorientations (Figs DR16, DR17). The feldspar aggregate also contains several isolated low- and high-Ca pyroxene grains with curved grain boundaries

(Fig. DR16). These grains do not preserve any significant intragrain misorientation (Fig. DR17). However, the large olivine grain in particle #0013 preserves an intragrain misorientation of approximately 6°, predominantly accommodated by low-angle (<10°) boundaries (Fig. DR16B).

Several plagioclase grains (n = 3), and all of the low-Ca pyroxene (n = 2), high-Ca pyroxene (n = 6) and the large olivine grain preserve a very strong crystallographic alignment with one another, such that {100} and {010} are coincident to within ~10° (Fig. DR17). All of the pyroxene grains exhibit the orientation of a single crystal, irrespective of their composition (Fig. DR17).

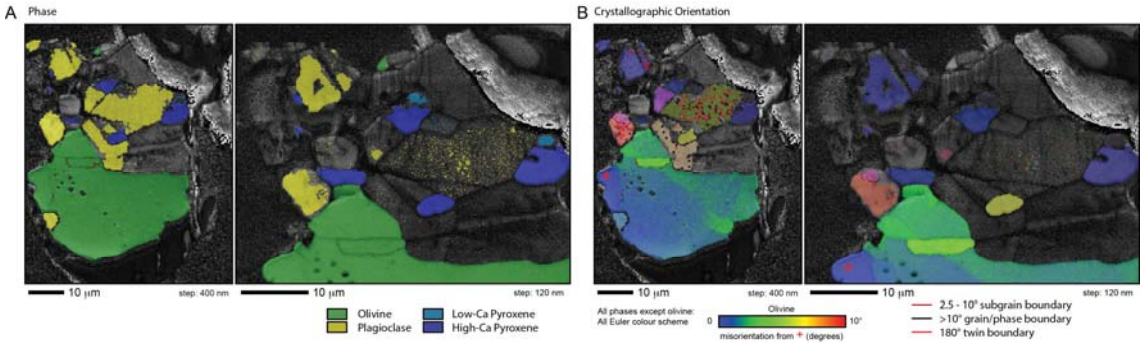

Fig. DR16: *EBSD maps coloured for (a) phase and (b) crystallographic orientation. Olivine in (b) coloured to show intragrain misorientation from reference spot (red cross) from 0 (blue) to 10° (red).*

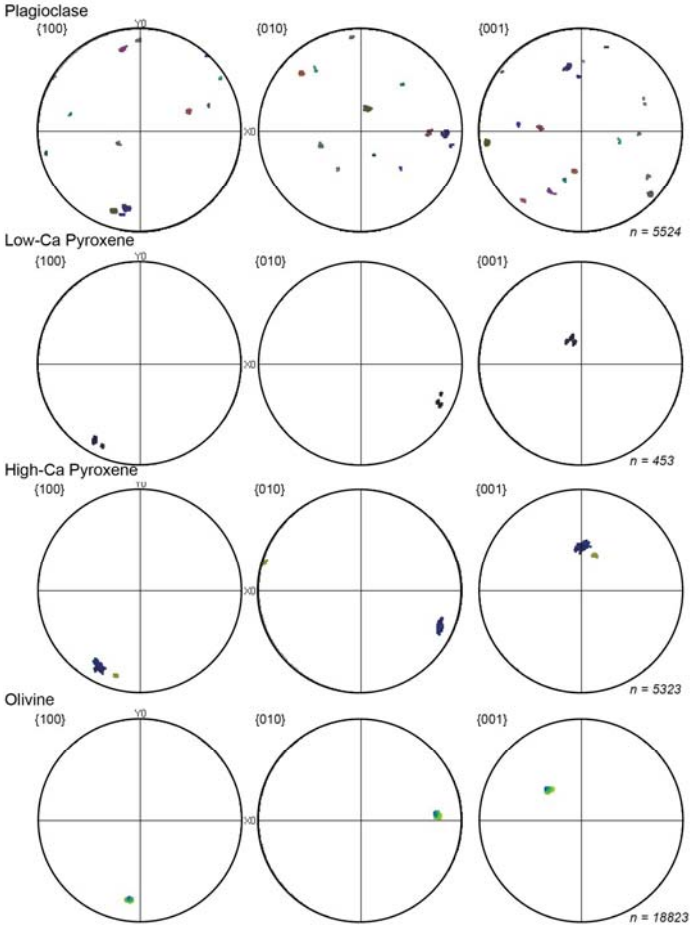

Fig. DR17*: Pole figures showing crystallographic orientation of data from different phases within particle #0013. Colours link to those shown in Fig. DR16B, except olivine, which is linked to Fig. 16A . Lower hemisphere, equal area stereographic projections.*

3.2 $^{40}Ar/^{39}Ar$ data

3.2.1 Particle RA-QD02-0030

The particle #0030 yielded a very low Ar signal beam with a total signal of 99 and 0.015 fA of ^{40}Ar* and ^{39}Ar, respectively, unfortunately making the age calculation extremely sensitive to the blank correction. Various blank reductions were applied giving apparent plateau ages of 4.6 ± 1.7 Ga (MSWD=0.9; P=0.58); 5.4 ± 1.6 Ga (MSWD=0.1; P=1.0) and a mini-plateau (impossible) age of e.g. 6.5 ± 0.6 Ga (Fig. DR18). Mini-plateaus are much less robust than their plateau counterparts (Jourdan et al., 2009) and in such a case, the impossible mini-plateau age is not discussed further. Such high ^{40}Ar*/^{39}Ar ratios given by the two plateaus are indicative either of a very old age (i.e., ~4.5 Ga) or excess ^{40}Ar*. Inverse isochron anlaysis cannot be used to determine the ^{40}Ar/^{36}Ar due to the clustering of the data near/at the radiogenic x-axis (Fig. DR19), but such a clustering indicates that no or very little excess Ar* is present in the sample, as otherwise, this would yield to a spread along the isochron line

(Jourdan et al., 2009). Although we cannot put with confidence an absolute age on this particle, we can determine that it is very old and much older than particle #0013 (cf. below). In any case, the importance of this particle resides in its complete lack of shock and this is consistent with this interpretation as extremely low level of shock would not reset the K/Ar systematics of this particle. Therefore, based on a total absence of shock (and to some extent on the old age given by the $^{40}Ar/^{39}Ar$ data), we conclude that particle #0030 must have an age around ~4.5 Ga similar to the most unshocked LL-chondrite (Bogard, 2011).

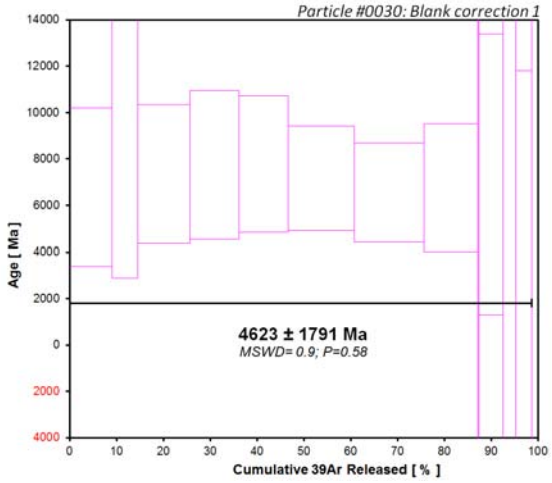

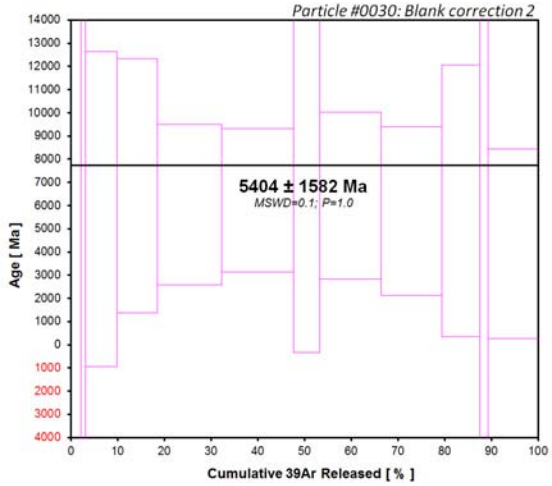

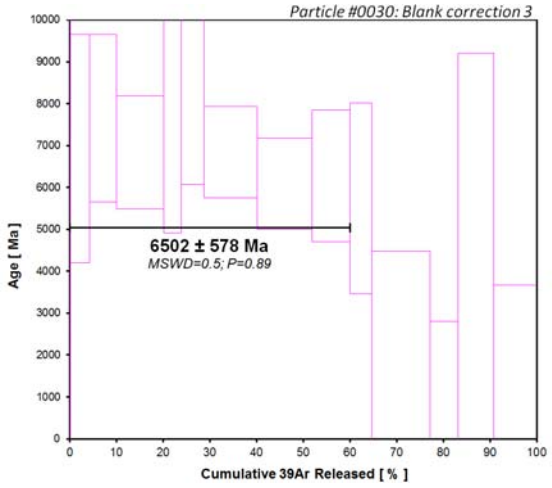

Fig. DR18: *$^{40}Ar/^{39}Ar$ age spectra of particle #0030 depending on blank corrections. The signal is very low and extremely sensitive to blank corrections making the exact age uncertain. Nevertheless, all solutions yield a very old age. The age has been calculated using a $^{40}Ar/^{36}Ar$ intercept ratio of 1±1.*

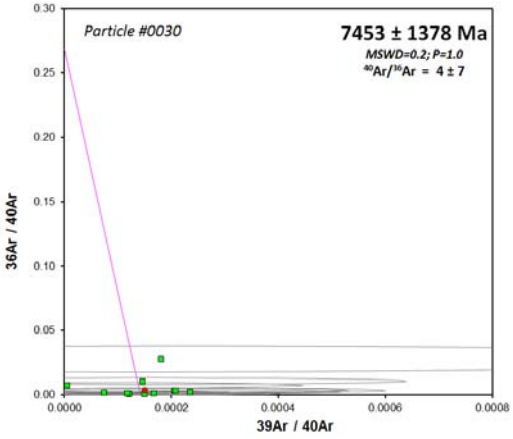

Fig. DR19: *Inverse isochron plot for 100% of the ^{39}Ar gas. The spreading factor (Jourdan et al., 2009) of the significant data points is less than 5% and the very large uncertainties of $^{40}Ar/^{39}Ar$ ratio is shown by the large ellipses along the x-axis.*

S3-A (blank correction 1)

J = 0.00665100 ± 0.00002422 Mass discrimination = 0.99455 ± 0.05% Only steps with a positive 39Ar value are shown

Relative Abundances			36Ar [pA]	%1σ	37Ar [pA]	%1σ	38Ar [pA]	%1σ	39Ar [pA]	%1σ	40Ar [pA]	%1σ	40(r)/39(k) ± 2σ	Age ± 2σ (Ma)	40Ar(r) (%)	39Ar(k) (%)
4M1183	1.7%	4	0.0000224	22.238	0.0000038	114.354	0.0000031	52.293	0.0000014	96.134	0.0065796	5.126	4809 ± 9280	6784.15 ± 3406.98	98.70	9.04
4M1184	1.8%	4	0.0000224	25.690	0.0000024	212.961	0.0000040	32.896	0.0000000	159.154	0.0110960	3.047	13232 ± 42213	8507.01 ± 5710.20	99.27	5.57
4M1186	1.9%	4	0.0000108	47.051	0.0000047	100.621	0.0000035	41.776	0.0000017	84.127	0.0110722	3.054	6645 ± 11211	7357.01 ± 2998.29	99.68	11.11
4M1187	2.0%	4	0.0000134	40.134	0.0000044	107.426	0.0000030	54.936	0.0000016	89.528	0.0130259	2.588	8288 ± 14876	7750.32 ± 3200.76	99.63	10.48
4M1189	2.2%	4	0.0000179	29.715	0.0000044	128.041	0.0000033	51.499	0.0000016	82.177	0.0132949	2.541	8414 ± 13864	7777.37 ± 2938.95	99.50	10.52
4M1190	2.4%	4	0.0000165	32.695	0.0000059	86.704	0.0000032	51.459	0.0000021	63.441	0.0126251	2.693	5905 ± 7616	7171.11 ± 2257.34	99.52	14.05
4M1192	2.6%	4	0.0000227	22.415	0.0000063	86.089	0.0000052	29.162	0.0000022	60.358	0.0095153	3.543	4227 ± 5123	6556.68 ± 2132.04	99.14	14.93
4M1193	2.8%	4	0.0000286	18.015	0.0000049	105.487	0.0000045	36.520	0.0000017	77.856	0.0082745	4.069	4761 ± 7440	6766.49 ± 2758.56	98.69	11.48
4M1195	3.1%	4	0.0000413	12.685	0.0000000	10160.930	0.0000053	31.938	0.0000000	3966.776	0.0058058	5.807	175196 ± 1391226	13243.36 ± 143490.32	97.25	0.22
4M1196	3.5%	4	0.0000551	9.278	0.0000022	224.944	0.0000066	25.415	0.0000008	169.814	0.0053759	6.280	6620 ± 22551	7350.27 ± 6053.76	96.01	5.22
4M1198	3.8%	4	0.0000593	9.228	0.0000012	442.299	0.0000070	24.105	0.0000004	344.693	0.0022460	14.990	4961 ± 34329	6839.00 ± 12227.16	89.72	2.72
4M1199	4.2%	4	0.0000106	48.301	0.0000015	298.397	0.0000008	194.374	0.0000005	273.874	0.0001373	244.882	187 ± 1584	1737.99 ± 10072.86	69.11	3.40
4M1201	4.6%		0.0000030	169.095	0.0000006	725.953	0.0000011	130.276	0.0000002	719.319	0.0000674	499.431	438 ± 7250	0.00 ± 40607.53	123.72	1.27

S3-B (blank correction 2)

J = 0.00865100 ± 0.00002422 Mass discrimination = 0.99455 ± 0.05% Only steps with a positive 39Ar value are shown

Relative Abundances			36Ar [pA]	%1σ	37Ar [pA]	%1σ	38Ar [pA]	%1σ	39Ar [pA]	%1σ	40Ar [pA]	%1σ	40(r)/39(k) ± 2σ	Age ± 2σ (Ma)	40Ar(r) (%)	39Ar(k) (%)
4M1180	1.5%	4	0.0000080	53.304	0.0000494	14.365	0.0000007	805.102	0.0000004	574.939	0.0003573	22.284	854 ± 10693	3846 ± 19917	97.56	2.13
4M1181	1.6%	4	0.0000286	13.560	0.0000447	13.191	0.0000014	386.883	0.0000002	1167.913	0.0034447	2.252	19661 ± 511046	9204 ± 49214	99.08	0.97
4M1183	1.7%	4	0.0000029	125.772	0.0000440	13.369	0.0000010	299.202	0.0000013	190.995	0.0036252	2.109	2810 ± 11025	5847 ± 6795	99.07	6.04
4M1184	1.8%	4	0.0000027	179.074	0.0000534	11.941	0.0000002	3340.664	0.0000017	151.778	0.0081267	0.993	5018 ± 15592	6860 ± 5490	99.96	8.61
4M1186	1.9%	4	0.0000787	19.420	0.0000571	10.828	0.0000014	372.260	0.0000026	97.630	0.0080627	1.026	3138 ± 6223	6034 ± 3459	100.25	13.71
4M1187	2.0%	4	0.0000034	121.978	0.0000409	12.559	0.0000019	280.959	0.0000029	97.281	0.0100304	0.777	3402 ± 6151	6216 ± 3092	100.02	15.34
4M1189	2.2%	4	0.0000064	65.668	0.0000512	13.515	0.0000017	316.432	0.0000011	225.938	0.0102712	0.797	9552 ± 44613	8004 ± 8344	100.06	5.73
4M1190	2.4%	4	0.0000060	86.328	0.0000546	11.871	0.0000018	297.816	0.0000025	100.918	0.0096821	0.836	3931 ± 8058	6429 ± 3601	100.04	13.13
4M1192	2.6%	4	0.0000004	1095.281	0.0000566	11.867	0.0000001	5296.232	0.0000025	102.909	0.0065139	1.203	2682 ± 5612	5762 ± 3627	100.01	12.92
4M1193	2.8%	4	0.0000047	93.940	0.0000485	13.336	0.0000005	1001.553	0.0000016	163.493	0.0052450	1.472	3452 ± 11544	6201 ± 5950	99.89	8.08
4M1195	3.1%	4	0.0000154	26.538	0.0000469	12.485	0.0000002	3049.659	0.0000004	674.381	0.0027703	2.870	8161 ± 120888	7723 ± 26409	99.37	1.79
4M1196	3.5%	4	0.0000277	14.037	0.0000510	12.291	0.0000014	381.276	0.0000021	121.821	0.0023858	3.340	1166 ± 2893	4350 ± 4081	98.72	10.75

S3-C (blank correction 3)

J = 0.00865100 ± 0.00002422 Mass discrimination = 0.99455 ± 0.05% Only steps with a positive 39Ar value are shown

Relative Abundances			36Ar [pA]	%1σ	37Ar [pA]	%1σ	38Ar [pA]	%1σ	39Ar [pA]	%1σ	40Ar [pA]	%1σ	40(r)/39(k) ± 2σ	Age ± 2σ (Ma)	40Ar(r) (%)	39Ar(k) (%)
4M1181	1.6%	4	0.0000488	5.109	0.0018288	0.260	0.0000072	18.634	0.0000013	46.783	0.0066981	0.916	93750 ± 5270108	12113.81 ± 101519.08	30.92	0.11
4M1183	1.7%	4	0.0000247	8.765	0.0015888	0.246	0.0000036	36.340	0.0000023	28.803	0.0067923	0.957	5200 ± 8014	6922.35 ± 2725.94	65.87	4.16
4M1184	1.8%	4	0.0000229	15.606	0.0020299	0.271	0.0000052	23.199	0.0000026	25.006	0.0113100	0.610	7040 ± 6769	7651.30 ± 1997.41	62.28	5.73
4M1186	1.9%	4	0.0000109	22.208	0.0021457	0.251	0.0000039	27.316	0.0000036	21.948	0.0112857	0.613	4940 ± 3769	6934.27 ± 1346.12	92.74	10.22
4M1187	2.0%	4	0.0000185	16.015	0.0019644	0.264	0.0000034	38.674	0.0000022	38.587	0.0132451	0.488	14923 ± 32336	8802.68 ± 3887.81	87.41	3.75
4M1189	2.2%	4	0.0000166	17.345	0.0019634	0.309	0.0000037	37.112	0.0000024	27.254	0.0135809	0.491	12118 ± 15937	8429.41 ± 2355.48	89.37	4.84
4M1190	2.4%	4	0.0000149	20.160	0.0021315	0.268	0.0000036	36.317	0.0000038	18.449	0.0120586	0.561	4961 ± 3059	6838.95 ± 1089.29	90.14	11.29
4M1192	2.6%	4	0.0000217	11.420	0.0021269	0.261	0.0000056	19.940	0.0000039	19.013	0.0097538	0.661	3228 ± 2019	6083.73 ± 1091.99	90.96	11.02
4M1193	2.8%	4	0.0000268	9.759	0.0020159	0.278	0.0000050	26.397	0.0000031	23.839	0.0085159	0.726	3611 ± 3240	6279.95 ± 1572.24	71.30	8.12
4M1195	3.1%		0.0000378	7.153	0.0018726	0.253	0.0000058	23.269	0.0000023	26.085	0.0060612	1.063	2640 ± 3477	5734.23 ± 2281.40	41.37	4.59
4M1196	3.5%		0.0000533	4.680	0.0020761	0.261	0.0000071	18.679	0.0000040	15.294	0.0056347	1.181	205 ± 466	1845.59 ± 2628.31	9.39	12.46
4M1199	3.8%		0.0000564	5.778	0.0018700	0.295	0.0000076	17.772	0.0000035	33.661	0.0025107	2.497	2322 ± 3436	0.00 ± 2866.97	114.07	6.01
4M1198	4.2%		0.0000061	39.954	0.0019049	0.252	0.0000014	83.710	0.0000029	28.922	0.0004084	14.672	52 ± 360	1093.43 ± 10300.96	20.47	7.70
4M1201	4.6%		0.0000008	325.561	0.0018843	0.244	0.0000002	530.184	0.0000032	22.487	0.0002477	25.158	107 ± 306	1187.35 ± 2483.84	82.46	9.20

Table DR3. $^{40}Ar/^{39}Ar$ data summary for sample #0030. Relative abundance values are corrected for mass discrimination, blanks, and radioactive decay. Measurement uncertainties are given at the 1σ level. Units in the tables are given in pA. Only steps with positive ^{39}Ar values are given for A,B and C. Due to the low signal, age calculation are very sensitive to blank corrections hence data using several blank corrections differing in the blank regression approach used, are given for transparency. **A.** Blank correction #1, **B.** Blank correction #2, **C.** Blank correction #3.

3.2.2 Particle RA-QD02-0013

Particle #0013 yielded a similar ^{40}Ar beam signal than particle #0030 with a value of 93 fA, but a much better ^{39}Ar signal with a value of 0.15 fA which is 10 times more than for particle #0030. Inverse isochron given by 94% of the total ^{39}Ar released yield an age of 2284 ± 220 Ma (2σ uncertainties) and an $^{40}Ar/^{36}Ar$ intercept of 52 ± 13 (2σ), with a MSWD = 1.0 and P-value of 0.39 (Fig. DR20). When using the measured $^{40}Ar/^{36}Ar$ intercept value for the trapped ratio, we calculate a plateau age of 2291 ± 139 Ma (MSWD=0.31; P=1.0) including 100% of the total ^{39}Ar released (Fig. DR21) and accounting for the uncertainties of the $^{40}Ar/^{36}Ar$ intercept. The plateau age of 2.29 ± 0.14 Ga is the age used in the discussion.

The age spectrum (Fig. DR13) shows two separate spikes of ^{39}Ar released separated by an area of low gas yield at intermediate temperatures. The two spikes are likely associated with the argon release first from the ca. 5 µm domain sized K-feldspar and subsequently from the 25 µm albite crystals (Fig. DR21), the latter having a higher activation energy than K-feldspar (Cassata and Renne, 2013). This is further demonstrated by our diffusion models (cf. below). The fact that the two phases yield the same apparent age within error give us confidence, first in the validity of this age and second that this age is associated with a thermal event that completely reset the K/Ar systematic of all the component of particle

#0013. It also dismiss the possibility of an age bias due to ^{39}Ar and ^{37}Ar nuclear recoil loss (Jourdan et a., 2007 and references inside) as the two phase with two different size yielded the same age.

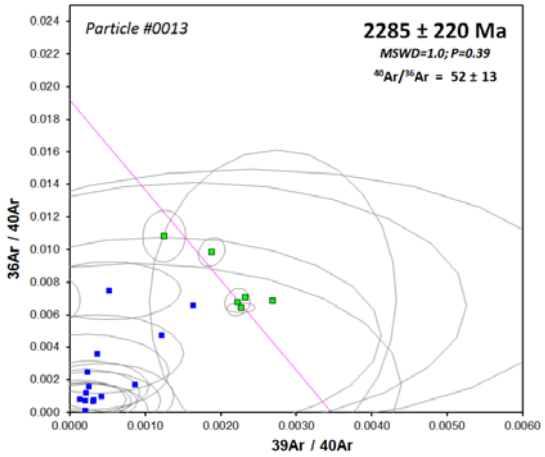

Fig. DR20: *Inverse isochron plot. The inverse isochron includes 94% of the total ^{39}Ar gas released (green-filled square). Data in blue have a very small signal at the background level and are excluded of the calculation. The spreading factor (Jourdan et al., 2009) of the significant data points is 24%.*

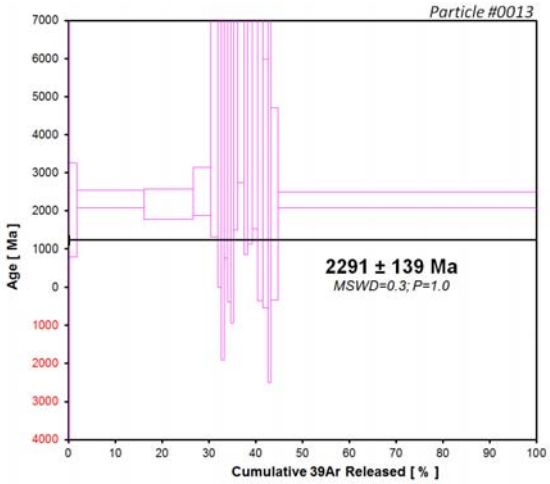

Fig. DR21: *Age spectrum of particle #0013 showing a 100% plateau age at ~2.29 Ga.*

J = 0.00878900 ± 0.00001089 Mass discrimination = 0.99455 ± 0.05%

Relative Abundances			36Ar [pA]	%1σ	37Ar [pA]	%1σ	38Ar [pA]	%1σ	39Ar [pA]	%1σ	40Ar [pA]	%1σ	40(r)/39(k) ± 2σ	Age ± 2σ (Ma)	40Ar(r) (%)	39Ar(k) (%)
4M1228	0.2%		0.0000012	240.875	0.0000006	785.758	0.0000003	586.311	0.0000003	218.332	0.0000317	242.007	188 1636	0.00 ± 39923.43	175.10	0.20
4M1229	0.4%	4	0.0000059	59.892	0.0000053	101.016	0.0000008	153.951	0.0000024	29.366	0.0000789	7.751	237 ± 239	2035.54 ± 1231.09	63.73	1.56
4M1231	0.6%	4	0.0000663	5.117	0.0000484	9.554	0.0000131	12.457	0.0000219	3.276	0.0009434	1.596	295 ± 52	2313.05 ± 230.44	64.02	14.44
4M1232	0.8%	4	0.0000820	3.283	0.0000350	9.925	0.0000139	12.184	0.0000158	4.216	0.0008836	2.019	264 ± 82	2178.76 ± 394.08	48.57	10.43
4M1234	1.0%	4	0.0000493	6.242	0.0000128	34.886	0.0000068	18.686	0.0000058	11.216	0.0004231	1.693	341 ± 169	2586.48 ± 630.04	42.63	3.82
4M1235	1.2%	4	0.0000017	9.786	0.0000049	92.611	0.0000058	25.743	0.0000022	92.037	0.0012857	2.002	1169 ± 2173	4379.89 ± 3063.24	60.41	1.46
4M1237	1.4%	4	0.0000022	27.536	0.0000027	100.699	0.0000021	91.004	0.0000012	158.051	0.0034143	2.157	2249 ± 7167	5484.64 ± 5484.88	60.92	0.81
4M1238	1.6%	4	0.0000007	40.791	0.0000019	211.932	0.0000012	145.451	0.0000008	235.902	0.0036579	1.903	3797 ± 17953	6395.95 ± 9300.24	66.93	0.55
4M1243	1.8%	4	0.0000058	58.106	0.0000026	169.611	0.0000008	4181.113	0.0000012	166.162	0.0055503	1.324	4375 ± 14567	6645.17 ± 5867.73	93.63	0.79
4M1244	2.0%	4	0.0000004	954.654	0.0000022	264.222	0.0000003	585.776	0.0000010	204.134	0.0047543	1.583	4888 ± 20833	6844.23 ± 7228.05	99.29	0.64
4M1246	2.2%	4	0.0000050	62.010	0.0000019	216.414	0.0000007	215.025	0.0000008	238.915	0.0064130	1.190	7446 ± 35640	7587.63 ± 8524.43	95.74	0.55
4M1247	2.4%	4	0.0000052	56.520	0.0000030	100.702	0.0000015	93.743	0.0000013	149.342	0.0066150	1.109	4727 ± 14145	6701.68 ± 5283.24	96.14	0.99
4M1249	2.6%	4	0.0000030	91.402	0.0000046	111.015	0.0000002	745.501	0.0000021	95.261	0.0067805	1.113	3146 ± 6006	6066.41 ± 3331.07	96.47	1.30
4M1250	2.8%	4	0.0000075	43.251	0.0000028	149.743	0.0000009	162.658	0.0000013	155.039	0.0049535	1.573	3607 ± 11207	6305.70 ± 5446.57	91.55	0.83
4M1252	3.0%	4	0.0000046	71.753	0.0000031	155.842	0.0000025	60.346	0.0000014	139.186	0.0044430	1.777	3017 ± 8419	5993.86 ± 4861.78	96.03	0.93
4M1253	3.2%	4	0.0000038	90.261	0.0000038	129.181	0.0000004	448.151	0.0000017	114.321	0.0041523	1.786	2264 ± 5279	5496.16 ± 3968.57	94.77	1.15
4M1255	3.4%	4	0.0000049	68.932	0.0000036	115.525	0.0000009	160.494	0.0000016	118.934	0.0013498	5.734	616 ± 1494	3359.83 ± 3702.95	74.97	1.09
4M1256	3.6%	4	0.0000064	52.694	0.0000039	117.290	0.0000003	436.095	0.0000010	110.629	0.0010760	7.110	400 ± 926	2724.81 ± 3260.63	65.14	1.16
4M1258	3.8%	4	0.0000025	136.174	0.0000022	189.534	0.0000012	162.399	0.0000010	204.024	0.0011159	6.718	1065 ± 4338	4211.49 ± 6712.38	90.97	0.64
4M1259	4.0%	4	0.0000071	42.453	0.0000048	111.646	0.0000019	81.725	0.0000022	92.333	0.0009429	8.412	269 ± 534	2181.84 ± 2524.31	62.47	1.45
4M1262	12%	4	0.0002508	1.860	0.0001905	2.231	0.0000572	3.753	0.0000861	4.065	0.0378780	0.443	231 ± 46	2292.66 ± 207.55	65.91	56.80
4M1264	14%		0.0000230	8.655	0.0000011	431.654	0.0000078	77.067	0.0000005	99.880	0.0036052	0.848	4748 9544	0.00 ± 3723.68	63.37	0.32
4M1265	16%		0.0000122	17.539	0.0000041	66.335	0.0000011	124.752	0.0000019	23.930	0.0006810	3.471	57 192	731.92 ± 2001.50	15.56	1.23

Table DR4. $^{40}Ar/^{39}Ar$ data summary for sample #0013. Relative abundance values are corrected for mass discrimination, blanks, and radioactive decay. Measurement uncertainties are given at the 1σ level. Units in the table are given in pA.

3.3 First $^{40}Ar/^{39}Ar$ analyses of single grain dust particles recovered from an extra-terrestrial body

We carried out $^{40}Ar/^{39}Ar$ analyses of two particles from Itokawa, with moderate success for particle #0030 (Fig. DR18) and complete success for particle #0013 (Fig. DR21). These data represent the first $^{40}Ar/^{39}Ar$ data ever obtained on single-grain dust particles recovered in-situ from an extra-terrestrial body and the first data on single particle of such a small size and low K_2O content. Therefore, the approach described above using an ultra-low-volume customized extraction line, a low-volume ARGUS VI mass spectrometer (Fig. DR12) (Phillips and Matchan, 2013) and measurements using a peak jumping approach on the CDD ion counter has been largely validated during this study. As a consequence, this study opens a new era of single grain analysis for precious, rare and small particles of extra-terrestrial material and should be applied to any future sample recovery mission (e.g. Hayabusa 2, Mars). Such an approach would not have been possible with the previous generation of noble gas machines (e.g., MAP 215-50; VG3600) as they were lacking sensitivity and their volume were too big (Matchan and Phillips, 2014). Only a multi-grain type analysis could allow recovering enough argon beam signal on those machines but, as shown in this study, since those particles do not come from a single sample, but rather from a regolith blanket including different particles with different shock-time-temperature histories, pooling several particles is not reasonable if one wants to recover usable information.

3.4 The power of the $^{40}Ar/^{39}Ar$ dating of regolith particles

A regolith layer consists of a myriad of detrital particles coming from various locations in the asteroid and mixed together by a large numbers of impacts of various sizes. This is well illustrated by our data showing two dust particles scooped together but showing completely different time-temperature histories. Here, our new approach means that each particle can deliver the time-temperature history from the rocks it belonged. Of course, two particles still

give only limited information regarding the history of an entire asteroid, but show that if one analyses a sufficient number of particles from a single scoop of the regolith, then one should be able to get a much better constraint on the global time-temperature history of an asteroid, maybe even more than a few decimetre-size samples from a single location. Terrestrial detrital studies showed that $^{40}Ar/^{39}Ar$ analyses of at least hundred crystals or so usually deliver a complete time-temperature history of the surrounding regions (Hodges et al., 2005). Since asteroids are likely to be less complex than terrestrial rocks, it is likely that only a fraction of this number is required to constrain the complete impact history of an asteroid. As a consequence, this study prompts us to recommend the targeting of regolith layers for future asteroid (and perhaps planet) recovery missions, especially since the approach pioneered in this study demonstrates that it is possible to analyse single dust particle.

Regarding Itokawa's particles, it would be desirable to analyse more dust particles. However, since the number of available dust particles with a *sufficient size* for $^{40}Ar/^{39}Ar$ dating is highly limited to a one or two tens of particles due to unexpected problems encountered during the Hayabusa probe sampling, and since the $^{40}Ar/^{39}Ar$ technique is a destructive method at the grain scale, our knowledge of the complete history of the asteroid will be limited to the $^{40}Ar/^{39}Ar$ dating of a few more particle at best (some in progress). Nevertheless, the dust samples recovered by the Hayabusa space probe give us an insight of what can be gained from complete regolith sample recovery.

4. Cooling and diffusion models

4.1 Stefan-Bolzman radiative cooling of a 25m radius boulder

We calculated the cooling time of a chondrite boulder of 25m radius from peak post-shock temperature to below 200°C. An average diameter of 25m has been chosen based on visual observation of Itokawa where boulders with a maximum size of 50m have been reported by (Tsuchiyama, 2014). We approximate the system by calculating the cooling time of a basaltic sphere in vacuum. The average physical properties of basalt are used as a proxy for chondritic material due to the larger availability of the physical constants of basalt within the current literature. The time scale required for radiative cooling was calculated after assuming an idealized perfect black body following Humayun and Koeberl (2004). This approximation is valid as the emissivity of basalt is measured to be higher than 0.95 at the high temperature regions (Ball and Pinkerton, 2006; Pinkerton et al., 2002):

$$\frac{dQ}{dt} = -C_p m \frac{dT}{dt} = 4\pi r^2 \sigma T^4 \qquad (1)$$

After substituting the density (ρ) and volume of the sphere $\left(\frac{4}{3}\pi r^3\right)$ by the mass $\left(m = \rho V = \rho \frac{4}{3}\pi r^3\right)$, and continuing with the separation of variables yields:

$$dt = \frac{-r\,\rho\,C_p}{3\sigma} T^{-4} dT \qquad (2)$$

The time elapsed since the starting point of the radiative cooling can be calculated after integrating the Equation (2) between the temperature limits of T when the time is equal to t, and the initial temperature as T_i at time zero:

$$\int_{t_0=0}^{t} dt = \frac{-r\rho\,C_p}{3\sigma} \int_{T_i}^{T} T^{-4}\, dT \qquad (3)$$

which yields the time (t) required for radiative cooling :

$$t = \frac{r\,\rho\,C_p}{9\sigma}\left[\frac{1}{T^3} - \frac{1}{{T_i}^3}\right] \qquad (4)$$

where r is radius of a sphere (m), ρ is density (kg/m^3), C_p is the heat capacity at constant pressure (j kg^{-1} K^{-1}), σ is the Stefan-Boltzmann constant (5.670373 × 10^{-8} kg s^{-3} K^{-4}), and T_i is the initial (maximum temperature) in Kelvin. The variables for the present system were taken as a sphere with r= 25 m; ρ for basalt was assumed to be around 3000 kg/m^3 (Leverington, 2007), and C_p of basalt was approximately 840 j kg^{-1} K^{-1} (Mitchell, 2005). The spherical solid particles of basalt at the beginning of the process (t_0=0 s) has an initial-maximum temperature of T_i where we used value of 900 and 500°C as iteratively calculated back and forth with the temperature calculated in our ^{40}Ar* diffusion model. The lower limit of our cooling model is set at 200°C where Ar stops to diffuse out of the system. Using equation (4), we calculated duration of 12.5 and 11.3 days for peak temperature of 900°C and 500C, respectively.

4.2 Solid-state diffusion of argon

Using solid-state diffusion models, we test the time-temperature conditions required to reset the K/Ar system in order to constrain the condition required to reproduce the reset age at 2.3 Ga for particle #0013.

We used the diffusion equations from (Crank and Gupta, 1975) with the details of the equations which are given by McDougall and Harrison (1999). We used spheres with a radius of 25 μm representing plagioclase crystals from particles #0030 and #0013 and a radius of 5 μm for the plagioclase exolutions.

When F ≤ 0.15 (e.g. (Crank and Gupta, 1975; McDougall and Harrison, 1999), the fraction of Ar retained in a spherical sample is given by:

$$F_{(sphere)} = 1 - f = (6/\pi^2) \cdot e^{\left(\frac{-\pi^2 \cdot D \cdot t}{r^2}\right)} \quad (5)$$

where f is the fraction of argon degassed, r is the radius of the sphere and t is the time required to achieve a given amount of Ar degassing. D is the diffusivity, whose temperature dependence is given by the Arrhenius relation:

$$D = D_0 \cdot e^{\left(\frac{-Ea}{\Re \cdot T}\right)} \quad (6)$$

where D_0 is the frequency factor and E_a is the activation energy for a given chemical composition and at a given pressure. R is the gas constant and T is the absolute maximum temperature of heating event.

We used the following diffusion parameters: Albite ($D_0 = 5 \times 10^3$ cm²/s; $E_a = 290$ kJ/mol), Kfeldspar ($D_0 = 5 \times 10^{-2}$ cm²/s; $E_a = 196$ kJ/mol) and orthopyroxene ($D_0 = 6 \times 10^2$ cm²/s; $E_a = 371$ kJ/mol) taken from Cassata and Renne (2013) and Cassata et al. (2011).

We calculate Ar-Time-temperature curves (A-T-t cuves, (Jourdan et al., 2010; Jourdan et al., 2014)) which represent the minimum time-temperature conditions required to fully purge the argon out of Albite and K-feldspar crystals with respective radius of 25 µm and 5 µm, respectively. In other words, our calculation illustrates the conditions required to completely reset the K/Ar system for those crystals. The time required to reset a given crystal varies in function of the temperature applied to the system with shorter durations required for higher temperatures. We indicated A-T-t curves calculated for duration of seconds, days and years for illustration. Our Stefan-Boltzmann cooling calculation (Eqn 4) suggests that a 25m boulder would take ca. 12 days to cool from 900°C to 200°C. The present diffusion model shows that for an albite crystal, a temperature of >800°C is necessary for a duration of ca. 11 days where the system is constantly maintained at this temperature (Fig. DR22b). Shorter durations (Fig. DR22a) are unlikely as the system requires time to cool down. Similarly, much longer durations (Fig. DR22c) are unlikely except if the particle is buried under an insulating regolith blanket that retards the loss of heat from the system. In this case, an overlong duration of 100 ka would still require a temperature of 500°C maintained for this duration (Fig. DR21c).

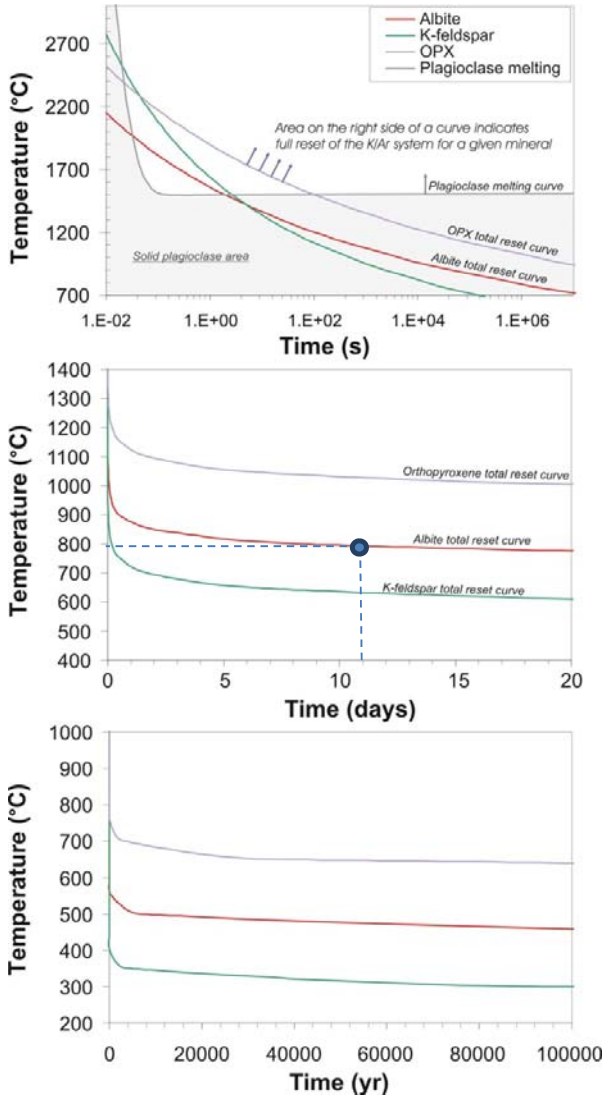

Fig. DR22*: A-T-t curves indicating the minimum time-temperature values needed to fully reset the K/Ar system for a sphere of 25 µm in radius (Jourdan et al., 2010). Areas located on the right or above the curve indicated full reset of the system for a given mineral. Red curve = albite, green curve = K-feldspar and purple curve = Orthopyroxene. D_0 and E_a values for each mineral are given in the text above. The three panes are the same graph plotted at different scale.*

Those calculations do not include a cooling history for the system (e.g., from 800°C to 200°C in 12 days) but rather assume a constant temperature maintained for a given duration (800°C maintained for 12 days), although the effect of the peak temperature is exponential (i.e. the value of the peak temperature for a given duration has more effect on the diffusion of Ar than the duration itself). Furthermore, this model does not take into account the radioactive decay accumulation of ^{40}Ar* between the time of crystallization and the shock reset event, nor the radiogenic ^{40}Ar*accumulation until present time. Lastly, it only provides the total argon loss of a single mineral phase rather than showing the effect of diffusion on a given age spectrum

produced from different mineral phases analysed together (i.e. here K-feldspar and albite). Therefore, we developed a more sophisticated model thereafter including cooling and radioactive decay and phase mixture resulting in synthetic $^{40}Ar/^{39}Ar$ age spectra to further test our hypotheses.

The overall fractional loss of ^{40}Ar (f) from a spherical geometry is calculated according to the following equation given by McDougall and Harrison (1999):

$$f = \frac{M_0 - M_f}{M_0} = 1 - 6\pi^{-2} \sum_{n=1}^{\infty} n^{-2} \exp\left(-\frac{Dn^2\pi^2 t}{r^2}\right) \qquad (7)$$

where M_0 is the initial mass of ^{40}Ar; M_f is the final mass of ^{40}Ar after a time interval of t, D is the diffusivity; and r is the effective diffusion radius of a spherical geometry and where argon diffusion in a mineral was assumed to follow the Arrhenius equation (Eqn 7).

The $^{40}Ar/^{39}Ar$ ratio observed in the laboratory after y-multiple outgassing events in nature for a duration of Δt_1 per each event, and a laboratory heating for a period of Δt^* was calculated according to the following formula modified after (McDougall and Harrison, 1999) to account for radioactive ingrowth from t_0 to present. C_j^* term represents the concentration of $^{40}Ar^*$ during each series of outgassing which includes the radioactive ingrowth of $^{40}Ar^*$ ands C_{39} is the unit value of ^{39}Ar concentration:

$$\frac{40_{Ar}}{39_{Ar}} = \sum_{j=1}^{y} \frac{C_j^*}{C_{39}} \left[\frac{\sum_{n=1}^{\infty} \exp\left(-\frac{n^2\pi^2 D(\Delta t_1 + \Delta t^*)}{r^2}\right)}{\sum_{n=1}^{\infty} \exp\left(-\frac{n^2\pi^2 D\Delta t^*}{r^2}\right)} \right] \qquad (8)$$

A versatile Excel spreadsheet has been developed for calculating the numerical solution of equations 7 and 8, leading to generate a theoretical $^{40}Ar/^{39}Ar$ spectra. For the infinite summation terms, 250 data points (from n=1 to n=250) have been used to simulate infinity.

We converted the $^{40}Ar/^{39}Ar$ ratio in apparent age (Ma) using the standard $^{40}Ar/^{39}Ar$ age equation and using a value of 1 for ^{39}Ar was calculated in parallel with the calculated amount of $^{40}Ar/^{39}Ar$ obtained from Eqn (8) :

$$Age = \frac{1}{\lambda} ln\left[1 + J_0\left(\frac{40_{Ar}}{39_{Ar}}\right)\right] \qquad (9)$$

where λ is the radioactive decay constant (5.54×10^{-10} year^{-1}), and J_o is a parameter related with the irradiation process. We tested our Excel model against available diffusion software (Lister and Baldwin, 1996) showing excellent match. However, the published version of this model is currently limited in its flexibility, in particular for simulation of impact-induced shock heating events which require peculiar conditions.

We interrogated our model for a series of T-t histories for each particle for Albite, K-feldspar, orthopyroxene and a mixture of 51:49% of Albite and K-feldspar. The goal was to test the maximum conditions that particle #0030 could withstand before its K/Ar system was sufficiently perturbed to yield an age significantly younger than the age spectrum obtained for this particle. We simulated a heating event at 2.3 Ga, but a heating event with any other age younger than ~ 4 Ga would have similar consequences for the particle. Conversely, we tested the minimum T-t conditions required to fully reset particle #0013 at 2.3 Ga.

4.2.1 Particle #0030

Diffusion models for a 25 µm radius albite crystal show that a maximum temperature of 500°C cooling down to 200°C in 11 days is allowed to account for the old age of the particle (Fig. DR23). For a much longer cooling duration of 100 ka (Fig. DR24), a maximum temperature of 350°C is allowed.

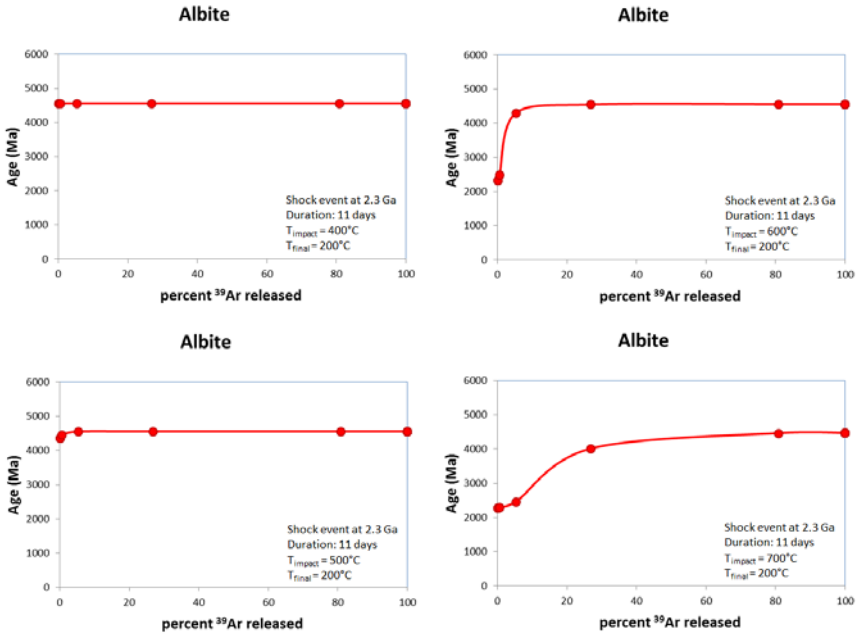

Fig. DR23: *Modelled age spectra for a 25 µm radius sphere with an albite composition (D_0 and E_a values are given in the text) that has been heated by impact shock at peak temperatures of 400 to 700°C. Cooling from the peak temperature to 200°C is simulated over 11 days.*

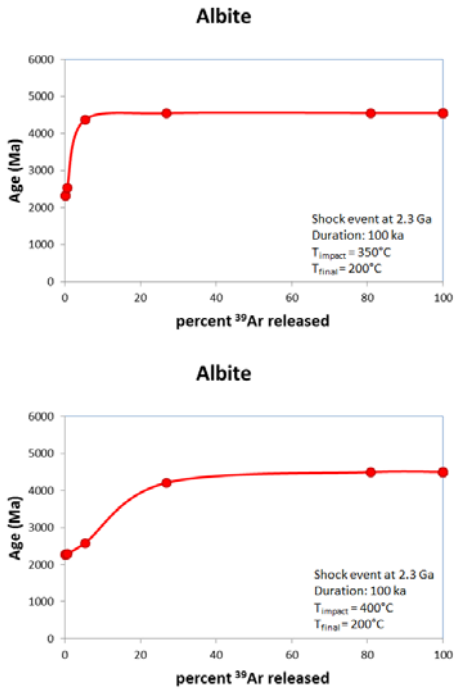

Fig. DR24: *Modelled age spectra for a 25 µm radius sphere with an albite composition (D_0 and E_a values are given in the text) that has been heated by impact shock at peak temperatures of 350 and 400°C. Cooling from the peak temperature to 200°C is simulated over 100,000 years.*

A relatively low temperature is in agreement with the total lack of shock evidence recorded by the particle and as demonstrated by the EBSD results (Fig. DR14).

4.2.2 Particle #0013

This particle has two main K reservoirs contributing to the ^{40}Ar* signal; the main crystal of albite, and the exolutions of K-feldspar. These crystals are approximated by spheres of 25 µm and 5 µm, respectively, and using the diffusion parameters given above. Modelling of the degassing behaviour of particle #0013 shows that two overlapping degassing peaks should be observed with the K-feldspar exolution degassing first (Fig. DR25). This is in agreement with a bimodal age spectrum (Fig. 2 and DR21) although the synthetic degassing curves suggest more overlap between the two phases, compared to the real age spectrum where the two degassing peaks are separated by a period of low gas yield at intermediate degassing temperatures. The ^{40}Ar/^{39}Ar spectra of an orthopyroxene crystal has been modelled for comparison, and our model shows a degassing event at much higher temperature.

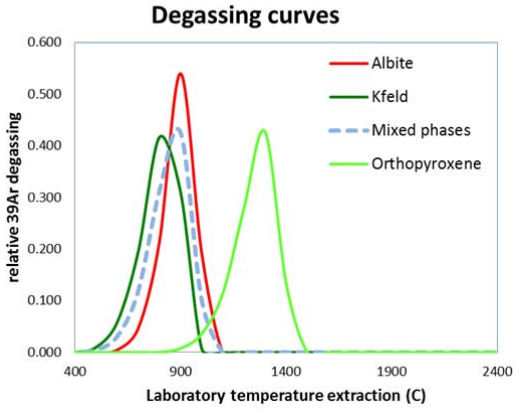

Fig. DR25. *Theoretical laboratory degassing curves for albite, K-feldspar and Orthopyroxene based on diffusion and sphere size given above. The dash curve represent the behavior of a particle including all those phases and relative to the amount of ^{40}Ar* given by each components. In this case, ^{40}Ar* is almost exclusively carried by albite and K-feldspar with a negligible contribution from Orthopyroxene.*

Our synthetic models show the theoretical behaviour of albite and K-feldspar in function of the peak temperature during a shock event and followed by cooling during 12.5 days (calculated below for a 25m radius boulder). The series of synthetic age spectra shows that albite is more resistant to such a heating event than K-feldspar, as K-feldspar is reset at 800°C whereas a temperature of 900°C is necessary to quasi-fully reset albite (Fig. DR26).

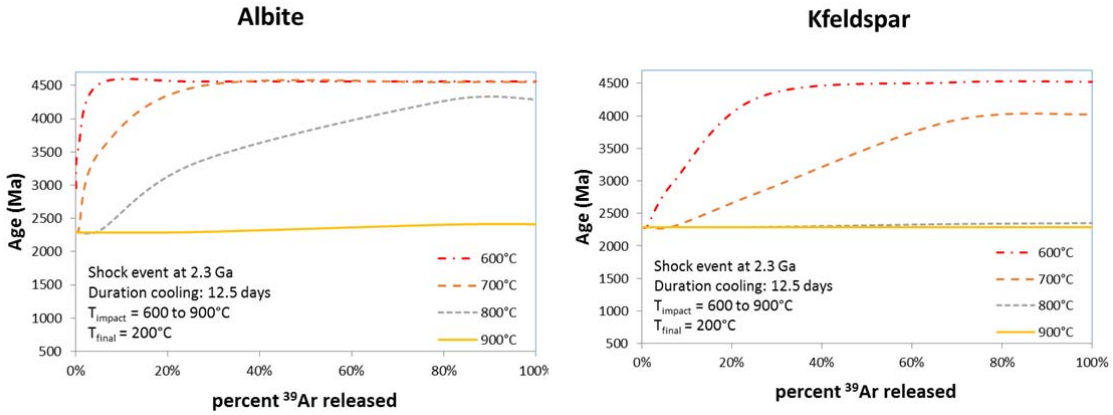

Fig. DR26: *Modelled age spectra for a 25 µm radius sphere with an albite composition and a 5µm radius sphere with a K-feldspar composition (D_0 and E_a values are given in the text) that has been heated by impact shock at peak temperatures of 600, 700, 800 and 900 °C. Cooling from the peak temperature to 200°C is simulated over 12.5 days.*

More importantly, we model the behaviour of a composite particle consisting of 51% albite and 49% K-feldspar and using the dimensions and diffusion parameters used above.

Complete reset is only reached at ~ 900°C as controlled by the more resistant albite crystal. This implies that the age spectrum obtained for particle #0013 can only be reproduced using temperature equal or in excess of 900°C (Fig. DR27).

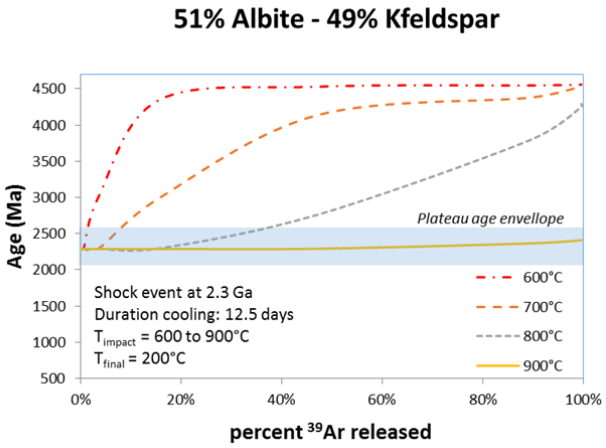

Fig. DR27: *Modelled age spectra for a mixture of a 25 µm radius sphere with an albite composition comprising 51% of the K_2O and a 5µm radius sphere with a Kfeldspar composition comprising 49% of the total K_2O (D_0 and E_a values are given in the text). The composite mixture has been heated by an impact shock at peak temperatures of 600, 700, 800 and 900 °C. Cooling from the peak temperature to 200°C is simulated over 12.5 days.*

If for some reason the cooling duration of the particle is significantly longer (e.g. improbable extreme case of 100 ka), then the temperature required to reset the albite-K-feldspar system will be lower than calculated above. Our model shows that a temperature of 500°C is required to purge the particle of its $^{40}Ar^*$ and reproduce the plateau spectrum of particle #0013 (Fig. DR21). We note that the later duration is totally unrealistic as an asteroid will behave like a black body and our calculation suggest that the post-shock cooling of small blocks happens in a matter of days/weeks, not 100 ka. Nevertheless, this shows that for such an improbable long cooling duration, even a 500°C peak temperature is incompatible with theoretical post-shock temperatures of 100-200°C associated with pressure of 15-25 GPa and based on Hugoniot curves (Schmitt et al., 1994).

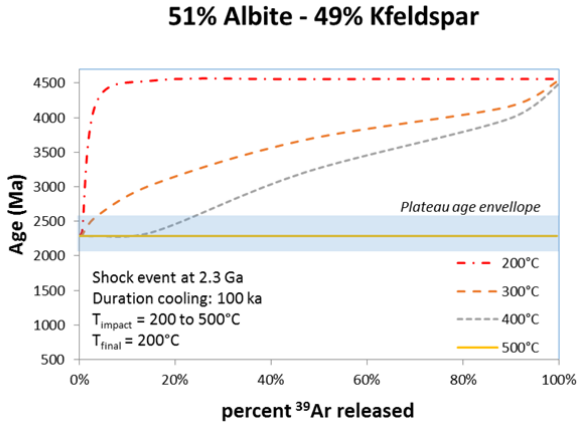

Fig. DR28. *Same caption as figure DR27 but for a cooling duration from peak temperature to 200°C of 100 ka (deemed unrealistic).*

4.3 Effect of porosity on post shock temperatures

The post-shock temperature required to reset the K/Ar system at 2.3 Ga has been calculated above to be around 900°C for a cooling duration of 12 days. The shock pressure required to cause such a post-shock temperature in an asteroid collision depends on the initial porosity of the asteroidal material. For a given shock pressure, porous rock is heated to a significantly higher temperature than nonporous rock (Davison et al., 2012; Davison et al., 2010; Wünnemann et al., 2008) owing to the extra waste heat from pore collapse. For example, Sharp and De Carli (2006) showed that non-porous quartz material shocked to 10 GPa experiences an increase in temperature of ca 75°C, whereas quartz sand with 40% porosity shocked to the same pressure is heated by more than 1500°C. To constrain shock heating of Itokawa-type material we calculated post-shock temperature as a function of shock pressure, with pressure values up to 70 GPa (Fig. 4) and up to 100 GPa (Fig. DR29)) and initial porosity (up to 40%) starting from a temperature of 0°C (cf. Eqn 10) and using the numerical approach described by Davison et al. (2010). Shock states, including entropies, were calculated by coupling the ANEOS equation of state (Melosh, 2007; Thompson and Lauson, 1972), the epsilon-alpha porous compaction model (Collins et al., 2011; Wünnemann et al., 2006) and the third Hugoniot equation, describing the conservation of energy during the jump from the reference state to the shock state. For each shock state the corresponding (post-shock) temperature after isentropic release was then computed using ANEOS by finding the 1-bar state at the same entropy as the shock state. To represent Itokawa material calculations used ANEOS input parameters for forsterite (Benz et al., 1989) and representative epsilon-alpha compaction model parameters for low-to-moderate porosity granular materials (Davison et al., 2010; Wünnemann et al., 2006; Davison et al., 2016). Our approach assumes hydrodynamic compression and so neglects shear heating owing to permanent shear deformation (although the dissipative effect of permanent compaction in porous materials is accounted for). This is an important additional component of shock heating in minerals at low (<20 GPa) pressure (Raikes and Ahrens (1979), but results in a temperature increase of <100°C. At higher pressure the relative contribution from shear heating is much smaller and the hydrodynamic approximation is sufficient. The results of our calculations (Fig. 4 and S29) are consistent with independent estimates of shock heating in L-chondrite analog materials (Schmitt et al., 1994; Schmitt, 2000). Note that Fig. DR29 provides solutions up to 100 GPa showing inflection in the P-T curves due to a phase transition in forsterite.

Assuming a shock pressure of 15-25 GPa (Schmidt, 2000) as indicated by the EBSD observations, our calculations suggest that a post-shock temperature of ca. 900°C requires an initial porosity of 20-30% in the host rock containing particle #0013 at the time of the impact. This is slightly lower than the present bulk porosity of Itokawa of ca. 40% (Tsuchiyama, 2014), but it is not clear what proportion of this bulk value is macro-scale porosity (e.g., large

fractures) versus micro-scale (e.g., intragrain) porosity likely to be present in the host rock of particle #0013. For a low (<5%) porosity material the same shock pressure would result in a very modest temperature increase (<150°C). Even for 10% porosity, which is the average porosity of Ordinary Chondrite meteorites after the initial asteroid compaction (Consolmagno et al., 2008), heating associated with shock pressures of 15-25 GPa is not expected to raise the temperature above 400°C. Therefore, it is clear that the target rocks must have had substantial porosity for moderate shock pressures to cause heating sufficient to reset the K/Ar system for both anorthite and K-feldspar. Such a high level of porosity is unlikely to be found on a post-compaction monolithic asteroid, or an asteroid with bulk properties consistent with Ordinary chondrite meteorites, but is consistent with the high-porosity rubble pile structure inferred for Itokawa. This implies that at the time of the impact at 2.3 Ga, the rubble pile structure of the asteroid was already formed. This asteroid could be Itokawa, or a larger version of Itokawa, but the monolithic parent asteroid had already been broken apart by a large impact prior to 2.3 Ga. Therefore, 2.3 Ga represents a minimum age for the formation of Itokawa's rubble pile structure.

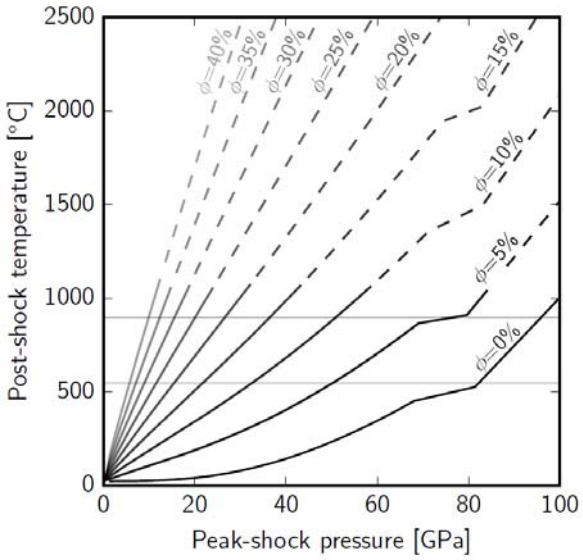

Fig. DR29: *Post-shock temperature of forsterite as a function of shock pressure for a range of different initial porosities (ϕ) and for peak shock pressure up to 100 GPa. Shock and release calculations computed using ANEOS equation of state for forsterite (Benz et al., 1989), following the approach described by (Davison et al., 2010). Temperatures above the solidus (dashed lines) are approximate as latent heat of fusion is neglected. Horizontal lines indicate the upper and lower bounds on heating inferred from K/Ar system resetting.*

4.4 Case for pyroxene $^{40}Ar^*$ contributions:

Chemical analyses suggest that up to ca. 0.4% of the K_2O in particle #0013 comes from low-Ca pyroxene (± olivine) which in this case, if potentially visible on an age spectra, would have required minimum temperatures of 1200°C for the same 12 days cooling duration to be

totally reset (Fig. DR30). This in turn suggests that the system would require a porosity of 40% for a shock pressure of 20 GPa. However, it is very unlikely that such a low $^{40}Ar^*$ contribution would be identifiable in a true step heating age spectrum and it is therefore safe to neglect any contribution from pyroxene in the $^{40}Ar/^{39}Ar$ age spectrum from particle #0013.

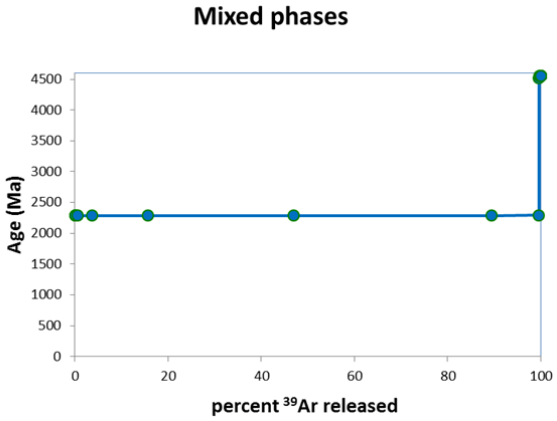

Fig. DR30*: Modelled age spectra for a mixture of a 25 µm radius sphere with an albite composition comprising 50.6% of the K_2O, a 5µm radius sphere with a Kfeldspar composition comprising 49% of the total K_2O and a 15 µm radius sphere with a Orthopyroxene composition and contributing to only 0.4% of the total K_2O (D_0 and E_a values are given in the text). The composite mixture has been heated by an impact shock at peak 900 °C and cooled to 200°C for 12.5 days. Only the last 0.4% of the age spectrum show the contribution of orthopyroxene which would be invisible on a real age spectrum.*

4.5 Effect of solar radiation on Ar diffusion loss and ambient temperature

4.5.1 surface temperature of Itokawa during its current orbit.

The two dust particles have likely been exposed to the surface of Itokawa since several million years as shown by cosmogenic exposure ages of up to 10 Ma (Nagao et al., 2011). During this time, the particles were exposed directly to the sun light and thus might have lost a portion of the $^{40}Ar^*$ due to diffusion. Itokawa' perihelion is similar to Earth's distance to the Sun, with a value of ~142 millions of km (0.95 AU). At this distance, without any atmosphere, and with an albedo of 0.24 and relatively fast rotation period of ca. 12 h, one can calculate a value for the equilibrium surface temperature of Itokawa.

$$T_{eq} = \frac{((As / (Ro)^2) \times 1-A \times (Ts)^4)}{4\pi^{0.25}} \qquad (10)$$

Where T_{eq} is the equilibrium temperature at the surface of Itokawa, As = area of the sun, A = bond albedo of Itokawa with a value of 0.24 (Cellino et al., 2005), T_s is the temperature of the sun (~6000 °K), and Ro is the radius of the Asteroid orbit (142 Mkm at its perihelion).

We calculate a maximum temperature 5 °C at perihelion. At a distance of 1 AU from the sun, this corresponds to a calculated temperature of -2 °C. The latter average value corresponds relatively well with recent spacecraft measurements that showed surface temperatures ranging from -15 °C to a peak temperature of 30 °C (Okada et al., 2006; Yano et al., 2006), and better describe the peak temperature experienced during day time compared to subsolar temperature calculations suggesting peak temperature of ca. 110°C.

Argon diffusion calculations using the diffusion equations described above and using the diffusion parameters previously mentioned for each mineral phase show that neither the albite grain (Equivalent radius of 25 µm and 48 µm spheres) nor the K-feldspar grain (with a radius of 5 µm) lose any radiogenic $^{40}Ar^*$ due to solar radiation ($T_{max\ Surface}$ ~ 30°C since the impact) at the surface of the asteroid for any period of time (Fig. DR29). Similar conclusions using different a diffusion modelling approach have been reached by Park et al. (2015).

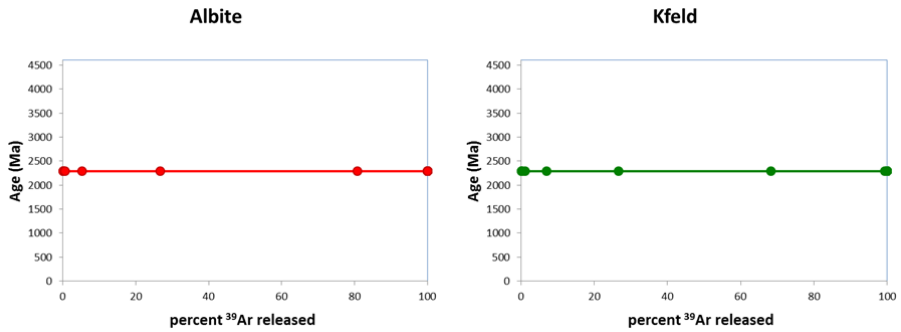

Fig. DR29: diffusion calculation showing the nil effect of Sun exposure on 2.3 Ga crystals of albite (25 µm radius) and K-feldspar (5 µm radius) and maintained at -2°C for 2.3 Ga.

Using the same equations, we have also calculated that the temperature reached during neutron irradiation and extraction line bake out (T_{max} ~ 250 °C for 75h) caused less than 0.004% of argon loss, hence fully preserving the information of impact events at the surface of the asteroid.

4.5.2 Sub-surface temperatures of Itokawa during past (mercurian?) orbit.

It has been proposed that the paleo-orbit of Itokawa could have taken the asteroid much closer to the Sun than its current orbit, and possibly as close as the current orbit of Mercury (Yoshikawa, 2002). Being so close to the sun would have an effect on the maximum temperature experienced by the two particles analyzed in this study and which could in turn affect the significance of the porosity calculation model presented above if the 2.3 Ga impact happened at 0.5 AU (the model assumes pre-shock temperature of 0 °C).

We have calculated a surface temperature of up to 212 °C at perihelion using an equilibrium temperature calculation presented in Eqn (9). As we have seen above, an equilibrium temperature calculation seems to better match the surface temperature measured on a relatively fast rotating body like Itokawa compared to a subsolar calculation, best used for slow rotating objects (e.g. the Moon), although it still requires an ad-hoc correction of +32 °C.

Whereas Eqn (9) works relatively well for estimating *surface temperatures*, cosmogenic exposure ages measured on several Itokawa's particles showed that the particles have been exposed to cosmic rays at the surface of the regolith for less than 10 Ma (Nagao et al., 2011). This means that Itokawa's particles were buried beyond the penetration depth of cosmic rays before then. Furthermore, considering that Itokawa is losing material with a thickness equivalent to tens cm / Ma (Nagao et al., 2011), it is safe to assume that the particles were all buried below (at very least) a few meters of regolith for the past several Ga. Therefore, since the peak temperature resulting from solar illumination is much lower at depth than at the very surface (Vasavada et al., 1999), that means that a depth-temperature attenuation factor (Jourdan and Eroglu, 2017) *must* be considered when calculating the temperature experienced by the particles. Vasavada et al. (1999) showed that below 80 cm depth, the temperature at the sub-surface of Mercury reaches an equilibrium temperature about 0.63 times (in °K) the temperature experienced by the surface of the body. For comparison, a similar equilibrium is reached below 30 cm on the Moon (Vasavada et al., 2012). If asteroid Itokawa would have followed an orbit close to Mercury's perihelion, we calculate that particles buried below 80 cm of regolith would experience a temperature of ca. 33 °C regardless if this temperature is measured during the day or night as the temperature reaches an equilibrium at this depth (Vasavada et al., 1999). Considering a bias of 32 °C between equilibrium temperature calculation and peak temperature measurement as shown in section 4.5.1, we estimate that the particle experienced a peak temperature of no more than 65°C. Significantly, such a temperature is too low to trigger any thermally activated Ar diffusion loss (cf. models above). Similarly, our temperature-shock porosity model assumes a pre-shock ambient temperature of 0 °C (Fig. 4). The ambient temperature range of buried particles from an asteroid on a mercurian orbit (~65 °C) or on Itokawa's current aphelion orbit (bias corrected temperature of -110 °C) correspond to porosity estimates that vary by less than 5% (Fig. 4 and DR29) for any range of shock pressure and, therefore, does not affect our estimates or conclusions.

4.6 Possibility of a transient event:

We now hypothesise that the peak temperature associated with the impact event at 2.3 Ga was not sustained for a period of more than a few tenths of a second and that the particles have cooled rapidly when exposed to the vacuum of space (Cassata et al., 2011). Solid-state diffusion modelling (Eqs 5 and 8) and thermodynamic melting calculations of plagioclase solidus as a function of time-temperature (Fig. DR22; Jourdan et al., 2014) predict that both a brief spike of temperature of *at least* ~2700°C sustained for at least 0.02s, followed by a virtually instantaneous cooling with a cooling rate of 8000°C/s are required in order to reset

the K/Ar clock of the plagioclase crystals *without* melting plagioclase (Fig. DR21). Such a high temperature requires either a very focussed energy wave, or a very high local porosity. It is not clear if the above conditions would irreversibly change the crystallographic structure of the crystal aggregate. Nevertheless, transient crystal melting calculations (cf. Fig. DR22 and Jourdan et al. (2014)) for crystal size of 1 µm to approximate crystal boundary dimensions show that for transient events longer than 0.02s, some crystals would show signs of melting at grain boundaries which has been observed for a few particles (e.g., #0032); but not for #0030 nor #0013 (Nakamura et al., 2011). Therefore, we rule-out any occurrence of a transient event due to the absence of melting evidence at grain boundaries within particles #0030 and #0013.

Supplementary text:

Comparison of our results with $^{40}Ar/^{39}Ar$ ages obtained for LL-chondrite

Analysis showed that Itokawa is a S-type asteroid body with a LL chondrite composition (Nakamura et al., 2011). LL-chondrites are the least abundant of all chondrite meteorites and only very few $^{40}Ar/^{39}Ar$ ages are available (Bogard, 2011), most of which are not based on plateau criteria. The $^{40}Ar/^{39}Ar$ age distribution of LL-chondrite show age concentration of > 3.8 Ga and < 1.3 Ga, with only one apparent age around 1.9 ± 0.1 Ga for the meteorite Parnallee (Ash et al., 1994; Swindle et al., 2014) which would be the only viable target in the terrestrial collection to have experienced an impact event with a distinctive apparent age sufficiently similar to the age given by the particle #0013 at 2.3 ± 0.1 Ga. We note that the apparent $^{40}Ar/^{39}Ar$ ages are statistically different but since the full dataset was not published, this makes the comparison between the latter data and the present results difficult. Nevertheless, this offers the interesting possibility that Paranallee could be an "Itokawite" meteorite and should be further investigated using modern $^{40}Ar/^{39}Ar$ approaches. Obviously, the $^{40}Ar/^{39}Ar$ age data bases of LL-chondrite and Itokawa grains are very poor and a priority task should be to analyse a significant amount of samples from both bodies. The lack of shock features and age resetting for particle #0030 make it not discriminatory in the LL-chondrite age database.

6. References (supporting material)

Ash, R. D., Gilmour, J. D., Turner, G., Bridges, J., and Hutchison, R., 1994, The chronology of ordinary chondrites by laser Ar-Ar and I-Xe: Meteoritics, v. 29, p. 439-440.

Ball, M., and Pinkerton, H., 2006, Factors affecting the accuracy of thermal imaging cameras in volcanology: Journal of Geophysical Research: Solid Earth, v. 111, p. B11203.

Benz, W., Cameron, A. G. W., and Melosh, H. J., 1989, The origin of the Moon and the single-impact hypothesis III: Icarus, v. 81, no. 1, p. 113-131.

Bogard, D. D., 2011, K-Ar ages of meteorites: Clues to parent-body thermal histories: Chemie Der Erde-Geochemistry, v. 71, no. 3, p. 207-226.

Cassata, W. S., and Renne, P. R., 2013, Systematic variations of argon diffusion in feldspars and implications for thermochronometry: Geochimica et Cosmochimica Acta, v. 112, p. 251-287.

Cassata, W. S., Renne, P. R., and Shuster, D. L., 2011, Argon diffusion in pyroxenes: Implications for thermochronometry and mantle degassing: Earth and Planetary Science Letters, v. 304, no. 3-4, p. 407-416.
Cellino, A., Yoshida, F., Anderlucci, E., Bendjoya, P., Di Martino, M., Ishiguro, M., Nakamura, A. M., and Saito, J., 2005, A polarimetric study of Asteroid 25143 Itokawa: Icarus, v. 179, no. 2, p. 297-303.
Collins, G. S., Melosh, H. J., and Wünnemann, K., 2011, Improvements to the ε-α Porous compaction model for simulating impacts into high-porosity solar system objects: International Journal of Impact Engineering, v. 38, no. 6, p. 434-439.
Consolmagno, G., Britt, D., and Macke, R., 2008, The significance of meteorite density and porosity: Chemie der Erde-Geochemistry, v. 68, no. 1, p. 1-29.
Crank, J., and Gupta, R. S., 1975, Isotherm Migration Method in 2 Dimensions: International Journal of Heat and Mass Transfer, v. 18, no. 9, p. 1101-1107.
Davison, T. M., Ciesla, F. J., and Collins, G. S., 2012, Post-impact thermal evolution of porous planetesimals: Geochimica et Cosmochimica Acta, v. 95, p. 252-269.
Davison, T. M., Collins, G. S., and Ciesla, F. J., 2010, Numerical modelling of heating in porous planetesimal collisions: Icarus, v. 208, no. 1, p. 468-481.
Davison T. M., Collins G. S., and Bland P. A. 2016. Mesoscale Modeling of Impact Compaction of Primitive Solar System Solids. *The Astrophysical Journal* 821:68.

Hodges, K. V., Ruhl, K. W., Wobus, C. W., and Pringle, M. S., 2005, 40Ar/39Ar thermochronology of detrital minerals, Reviews in Mineralogy and Geochemistry, Volume 58, p. 239-257.
Humayun, M., and Koeberl, C., 2004, Potassium isotopic composition of Australasian tektites: Meteoritics & Planetary Science, v. 39, no. 9, p. 1509-1516.
Jourdan, F., Andreoli, M. A. G., McDonald, I., and Maier, W. D., 2010, 40Ar/39Ar thermochronology of the fossil LL6-chondrite from the Morokweng crater, South Africa: Geochimica et Cosmochimica Acta, v. 74, no. 5, p. 1734-1747.
Jourdan, F., Benedix, G., Eroglu, E., Bland, P., and Bouvier, A., 2014, 40Ar/39Ar impact ages and time-temperature argon diffusion history of the Bunburra Rockhole anomalous basaltic achondrite: Geochimica et Cosmochimica Acta, v. 140, p. 391-409.
Jourdan, F., and Eroglu, E., 2017, 40Ar/39Ar and (U-Th)/He model age signatures of elusive Mercurian and Venusian meteorites: Meteoritics & Planetary Science.
Jourdan, F., and Renne, P. R., 2007, Age calibration of the Fish Canyon sanidine Ar-40/Ar-39 dating standard using primary K-Ar standards: Geochimica Et Cosmochimica Acta, v. 71, no. 2, p. 387-402.
Jourdan, F., Renne, P. R., and Reimold, W. U., 2009, An appraisal of the ages of terrestrial impact structures: Earth and Planetary Science Letters, v. 286, no. 1-2, p. 1-13.
Jourdan, F., Verati, C., and Feraud, G., 2006, Intercalibration of the Hb3gr Ar-40/Ar-39 dating standard: Chemical Geology, v. 231, no. 3, p. 177-189.
Koppers, A. A. P., 2002, ArArCALC - software for Ar-40/Ar-39 age calculations: Computers & Geosciences, v. 28, no. 5, p. 605-619.
Lee, J. Y., Marti, K., Severinghaus, J. P., Kawamura, K., Yoo, H. S., Lee, J. B., and Kim, J. S., 2006, A redetermination of the isotopic abundances of atmospheric Ar: Geochimica Et Cosmochimica Acta, v. 70, no. 17, p. 4507-4512.
Leverington, D. W., 2007, Was the Mangala Valles system incised by volcanic flows?: Journal of Geophysical Research: Planets, v. 112, p. E11005.

Lister, G. S., and Baldwin, S. L., 1996, Modelling the effect of arbitrary P-T-t histories on argon diffusion in minerals using the MacArgon program for the Apple Macintosh: Tectonophysics, v. 253, no. 1-2, p. 83-109.

Matchan, E. L., and Phillips, D., 2014, High precision multi-collector 40Ar/39Ar dating of young basalts: Mount Rouse volcano (SE Australia) revisited: Quaternary Geochronology, v. 22, p. 57-64.

McDougall, I., and Harrison, T. M., 1999, Geochronology and thermochronology by the 40Ar/39Ar method, Oxford, New York, Oxford University Press, Geochronology and thermochronology by the 40Ar/39Ar method, 269 p.:

Melosh, H. J., 2007, A hydrocode equation of state for SiO2: Meteoritics and Planetary Science, v. 42, no. 12, p. 2079-2098.

Mitchell, K. L., 2005, Coupled conduit flow and shape in explosive volcanic eruptions: Journal of volcanology and geothermal research, v. 143, no. 1, p. 187-203.

Nagao, K., Okazaki, R., Nakamura, T., Miura, Y. N., Osawa, T., Bajo, K.-i., Matsuda, S., Ebihara, M., Ireland, T. R., and Kitajima, F., 2011, Irradiation history of Itokawa regolith material deduced from noble gases in the Hayabusa samples: Science, v. 333, no. 6046, p. 1128-1131.

Nakamura, T., Noguchi, T., Tanaka, M., Zolensky, M. E., Kimura, M., Tsuchiyama, A., Nakato, A., Ogami, T., Ishida, H., Uesugi, M., Yada, T., Shirai, K., Fujimura, A., Okazaki, R., Sandford, S. A., Ishibashi, Y., Abe, M., Okada, T., Ueno, M., Mukai, T., Yoshikawa, M., and Kawaguchi, J., 2011, Itokawa dust particles: A direct link between S-type asteroids and ordinary chondrites: Science, v. 333, no. 6046, p. 1113-1116.

Nakashima, D., Kita, N. T., Ushikubo, T., Noguchi, T., Nakamura, T., and Valley, J. W., 2013, Oxygen three-isotope ratios of silicate particles returned from asteroid Itokawa by the Hayabusa spacecraft: A strong link with equilibrated LL chondrites: Earth and Planetary Science Letters, v. 379, p. 127-136.

Okada, T., Yamamoto, Y., Inoue, T., Shirai, K., Arai, T., Ogawa, K., Hosono, K., and Kato, M., Thermal radiometry of asteroid itokawa by the XRS onboard Hayabusa, *in* Proceedings 37th Annual Lunar and Planetary Science Conference2006, Volume 37.

Phillips, D., and Matchan, E. L., 2013, Ultra-high precision 40Ar/39Ar ages for Fish Canyon Tuff and Alder Creek Rhyolite sanidine: New dating standards required?: Geochimica et Cosmochimica Acta, v. 121, p. 229-239.

Pinkerton, H., James, M., and Jones, A., 2002, Surface temperature measurements of active lava flows on Kilauea volcano, Hawai′ i: Journal of volcanology and geothermal research, v. 113, no. 1, p. 159-176.

Raikes, S. A., and Ahrens, T. J., 1979, Post-shock temperatures in minerals: Geophysical Journal of the Royal Astronomical Society, v. 58, no. 3, p. 717-747.

Renne, P. R., Balco, G., Ludwig, K. R., Mundil, R., and Min, K., 2011, Response to the comment by W.H. Schwarz et al. on "Joint determination of K-40 decay constants and Ar-40*/K-40 for the Fish Canyon sanidine standard, and improved accuracy for Ar-40/Ar-39 geochronology" by PR Renne et al. (2010): Geochimica Et Cosmochimica Acta, v. 75, no. 17, p. 5097-5100.

Schmitt, R., Deutsch, A., and Stöffler, D., Calculation of Hugoniot curves and post-shock temperatures for H-and L-chondrites, *in* Proceedings Lunar and Planetary Institute Science Conference Abstracts1994, Volume 25, p. 1209.

Schmitt, R. T., 2000, Shock experiments with the H6 chondrite Kernouve: Pressure calibration of microscopic shock effects: Meteoritics and Planetary Science, v. 35, no. 3, p. 545-560.

Sharp, T. J., and De Carli, P. S., 2006, Shock Effects in Meteorites, *in* Lauretta, D. S., and Jr., H. Y. M., eds., Meteorites and the Early Solar System II: Tucson, University of Arizona Press, p. 653-677.

Swindle, T. D., Kring, D. A., and Weirich, J. R., 2014, 40Ar/39Ar ages of impacts involving ordinary chondrite meteorites, *in* Jourdan, F., Mark, D. F., and Verati, C., eds., Advances in 40Ar/39Ar Dating: from Archaeology to Planetary Sciences, Volume 378: London, Geological Society, p. 333-347.

Thompson, S., and Lauson, H., 1972, Improvements in the CHART D Radiation-hydrodynamic Code III: Revised Analytic Eauation of State.

Tsuchiyama, A., 2014, Asteroid Itokawa a source of ordinary chondrites and a laboratory for surface processes: Elements, v. 10, no. 1, p. 45-50.

Vasavada, A. R., Bandfield, J. L., Greenhagen, B. T., Hayne, P. O., Siegler, M. A., Williams, J. P., and Paige, D. A., 2012, Lunar equatorial surface temperatures and regolith properties from the Diviner Lunar Radiometer Experiment: Journal of Geophysical Research: Planets, v. 117, no. E12.

Vasavada, A. R., Paige, D. A., and Wood, S. E., 1999, Near-surface temperatures on Mercury and the Moon and the stability of polar ice deposits: Icarus, v. 141, no. 2, p. 179-193.

Wünnemann, K., Collins, G. S., and Melosh, H. J., 2006, A strain-based porosity model for use in hydrocode simulations of impacts and implications for transient crater growth in porous targets: Icarus, v. 180, no. 2, p. 514-527.

Wünnemann, K., Collins, G. S., and Osinski, G. R., 2008, Numerical modelling of impact melt production in porous rocks: Earth and Planetary Science Letters, v. 269, no. 3-4, p. 529-538.

Yano, H., Kubota, T., Miyamoto, H., Okada, T., Scheeres, D., Takagi, Y., Yoshida, K., Abe, M., Abe, S., and Barnouin-Jha, O., 2006, Touchdown of the Hayabusa spacecraft at the Muses Sea on Itokawa: Science, v. 312, no. 5778, p. 1350-1353.

Yoshikawa, M., Orbital evolution of the MUSES-C mission target:(25143) 1998 SF36, *in* Proceedings Asteroids, Comets, and Meteors: ACM 20022002, Volume 500, p. 331-333.

Yurimoto, H., Abe, K. I., Abe, M., Ebihara, M., Fujimura, A., Hashiguchi, M., Hashizume, K., Ireland, T. R., Itoh, S., Katayama, J., Kato, C., Kawaguchi, J., Kawasaki, N., Kitajima, F., Kobayashi, S., Meike, T., Mukai, T., Nagao, K., Nakamura, T., Naraoka, H., Noguchi, T., Okazaki, R., Park, C., Sakamoto, N., Seto, Y., Takei, M., Tsuchiyama, A., Uesugi, M., Wakaki, S., Yada, T., Yamamoto, K., Yoshikawa, M., and Zolensky, M. E., 2011, Oxygen isotopic compositions of asteroidal materials returned from Itokawa by the Hayabusa mission: Science, v. 333, no. 6046, p. 1116-1119.